

4

Permanent Magnet Brushless Motor Drives

Among various types of motor drives, permanent magnet (PM) brushless motor drives, especially the PM synchronous motor drive, are currently the most attractive motor drives for electric vehicle (EV) propulsion. Their key features, namely high power density and high efficiency, are attributed to the use of high-energy PM material. Actually, they are becoming dominant in the market share of EV motor drives. However, these PM brushless motor drives still have some shortcomings such as high cost and thermal instability of the PM material.

In this chapter, two major PM brushless motor drives, namely the PM synchronous and PM brushless DC (BLDC) types, are presented. Their PM materials, system configurations, machine topologies, inverter topologies, and control strategies are described. The corresponding design criteria, design examples, and application examples are also discussed for EV propulsion.

4.1 PM Materials

Definitely, PM materials are the key of PM brushless motor drives that provide the machines with lifelong excitation. The development of PM materials dates back over many centuries. As depicted in Figure 4.1, the progress of PM materials proceeded in a stepwise manner, and each PM material was developed and improved before being superseded by a new one (Gutfleisch, 2000). Particularly, the corresponding energy product has had a drastic improvement starting from the 1980s.

Currently, there are four major types of PM materials that are widely used for motor drives:

- **Ferrite:** The ferrite magnet was invented in the 1930s. It has been widely used as commercial magnets for the last few decades because of the abundance of raw materials and low production cost. It also offers the advantage of high electrical resistance, which can suppress the corresponding eddy-current loss. However, it suffers from drawbacks such as high temperature coefficient and low energy density, leading to be sensitive to temperature variations and bulky in size, respectively, for application to PM machines.
- **Alnico:** It is a nickname of iron-based aluminum-nickel-cobalt (Al-Ni-Co) alloy, which was invented in the 1940s. It was the first modern PM material offering high remanence. Because of its high Curie temperature, it can be used at high operating temperature. Unfortunately, its coercivity is very low so that it is very easy to be demagnetized, which limits the corresponding application to PM machines.

Electric Vehicle Machines and Drives: Design, Analysis and Application, First Edition. K. T. Chau.
© 2015 John Wiley & Sons (Asia) Pte Ltd. Published 2015 by John Wiley & Sons (Asia) Pte Ltd.

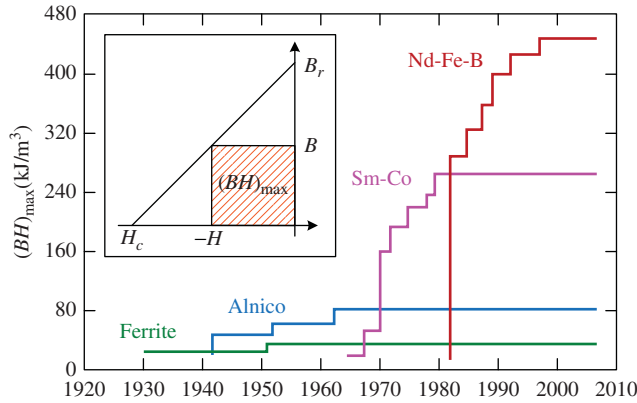


Figure 4.1 Development of PM materials

Nevertheless, some special machines, such as the memory machine, positively utilize this property so that the magnetization level can be online tuned.

- **Samarium-cobalt (Sm-Co):** Invented in the 1960s, this rare-earth PM material has merits such as high remanence, high coercivity, high energy density, high Curie temperature, and low temperature coefficient. It is well suited for application to PM machines, which desire high power density, high efficiency, and high stability. However, its cost is the key drawback. Particularly, the rare-earth element, samarium, is very expensive.
- **Neodymium-iron-boron (Nd-Fe-B):** First produced in 1984, this rare-earth PM material has better magnetic properties than samarium-cobalt. Since neodymium is a relatively less expensive rare-earth element, the corresponding cost becomes reasonable for application to PM machines. The relatively low Curie temperature (345 °C) is the major concern, which limits its use for high-temperature applications. Currently, this PM material is almost exclusively used for EV motor drives. Because of such an exponential growth in demand, the price is highly volatile, sometimes unreasonably expensive.

Figure 4.2 shows typical demagnetization characteristics of the above PM materials in which the remanence, B_r , denotes the strength of the magnetic field produced, and the coercivity, H_c , denotes the resistance to becoming demagnetized. The maximum product of an operating point on the characteristic is dubbed as the energy product $(BH)_{\max}$, which actually represents the corresponding energy density. Additionally, the PM properties are usually temperature-dependent, and vary according to the temperature coefficient. Exposure to a temperature called the Curie temperature, T_c , the PM material completely loses its magnetization. Therefore, the operating temperature range must be taken into account during the design of PM machines. A brief summary of typical PM properties is given in Table 4.1.

4.2 System Configurations

The system configuration of PM brushless motor drives for electric propulsion is similar to that of induction motor drives. Major alternatives such as single-motor and multiple-motor configurations as well as geared and gearless transmissions can be found. Basically, the single-motor system configuration consists of a PM brushless machine, a voltage-fed inverter, an electronic controller, and some sensors as shown in Figure 4.3. Nevertheless, there are some variations:

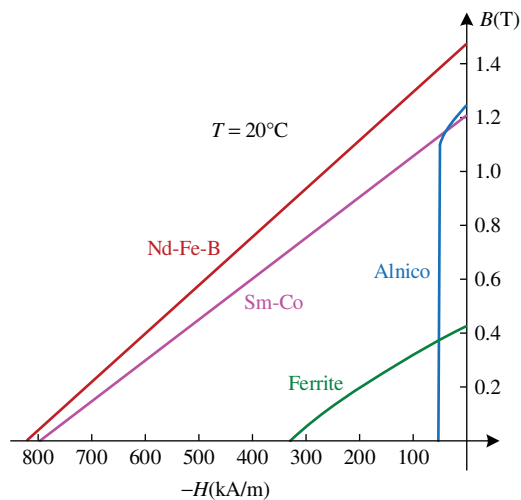


Figure 4.2 Demagnetization curves of PM materials

Table 4.1 Properties of PM materials

	Ferrite	Alnico	Sm-Co	Nd-Fe-B
Remanence, B_r (T)	0.43	1.25	1.21	1.47
Coercivity, H_c (kA/m)	330	51	796	820
Energy product, $(BH)_{\max}$ (kJ/m ³)	35	44	271	422
Temperature coefficient of B_r (%/°C)	−0.18	−0.02	−0.03	−0.11
Temperature coefficient of H_c (%/°C)	0.2	0.01	−0.22	−0.65
Curie temperature, T_c (°C)	450	860	825	345

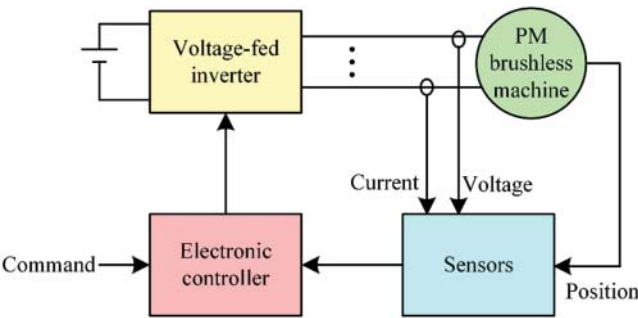


Figure 4.3 Basic configuration of PM brushless motor drive

- When the PM brushless machine is designed with sinusoidal distribution of air-gap flux and distributed arrangement of stator windings, the machine operates as a synchronous machine, the so-called PM synchronous machine or PM brushless AC (BLAC) machine. Similar to that for induction motor drives, the PM synchronous motor drive adopts sophisticated speed control strategies such as the field-oriented control (FOC) and direct torque control, which generally demand an expensive position sensor such as the absolute position encoder or resolver. Although this position sensor can be ignored theoretically for open-loop operation, this strategy is seldom adopted for EV propulsion.
- When the PM brushless machine is designed with trapezoidal distribution of air-gap flux and concentrated arrangement of stator windings, the machine operates like a DC machine but without brushes, the so-called PM BLDC machine. The corresponding speed control is relatively simple in which the stator currents are controlled in such a way that the rectangular current properly aligns with the trapezoidal flux. The position sensor is mandatory to ensure the synchronization of the current with the flux. The resolution requirement of this position sensor is not demanding since only six commutation instants are needed per electrical cycle. In general, a low-cost Hall position sensor is adopted.

4.3 PM Brushless Machines

The PM brushless machines have superseded induction machine in recent years, becoming the preferred machines for EV propulsion. Their major advantages are as follows:

- Since the magnetic field is excited by high-energy PMs, the overall weight and volume can be significantly reduced for a given output power, leading to higher power density.
- Because of the absence of rotor copper loss, they inherently offer higher efficiency.
- Since the heat mainly arises in the stator, it can be more efficiently dissipated to the surroundings, leading to easier cooling.
- As the PM excitation has no risk of manufacturing defects, overheating, or mechanical damage, they inherently offer higher reliability.
- Because of absence of copper windings in the rotor, they possess lower electromechanical time constant and hence better dynamic response.

However, these machines still suffer from some drawbacks as follows:

- Since the high-energy PMs are based on rare-earth elements, the machine cost is much higher than that of the induction counterpart.
- As the PMs are located in the rotor, the mechanical integrity of the rotor, especially the surface-mounted PM type, has a problem for high-speed operation.
- Because of the inherently uncontrollable PM flux, the constant-power operation range is limited.
- In case the machine is not properly designed or operated, the PMs may be accidentally demagnetized by high armature reaction field or under high operating temperatures.

The family of PM brushless machines has two main members: the PM synchronous machine and the PM BLDC machine. The PM synchronous machine has been widely used for EV propulsion; meanwhile, the PM BLDC machine is becoming attractive.

4.3.1 Structure of PM Brushless Machines

The basic structure of the PM brushless machine, including both the PM synchronous and PM BLDC types, is depicted in Figure 4.4. It mainly consists of a stator incorporated with the three-phase armature winding and a rotor incorporated with PM poles. Compared with the induction machine, it is relatively

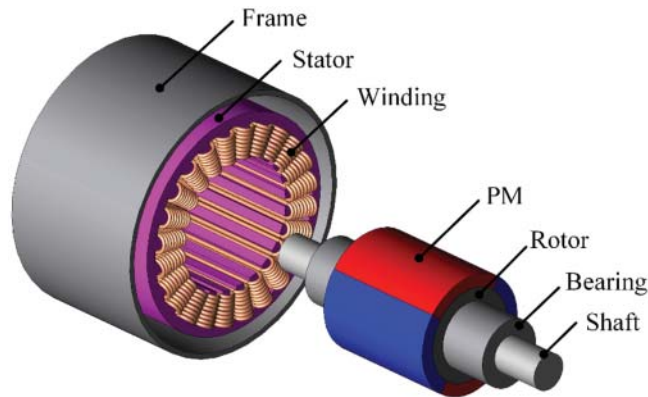


Figure 4.4 PM brushless machine exploded diagram

simpler because of the absence of cage bars and end-rings. In addition, since the associated heat loss in the rotor is not significant, it generally does not require to mount fan blades on the rotor or shaft for forced-air cooling.

4.3.1.1 PM Synchronous Machine Structure

By replacing the field winding of the wound-rotor synchronous machine with PM poles, the PM synchronous machine can readily be generated. Similar to the conventional synchronous machine, the stator has the three-phase distributed armature winding in the stator. When the armature winding is fed with three-phase sinusoidal currents, a synchronously rotating sinusoidal air-gap flux is created. Hence, the PM rotor with the same number of poles as the rotating air-gap flux always rotates in synchronism, which depends on the applied frequency.

On the basis of the placement of PMs in the rotor, the PM synchronous machine can be further classified as the surface-mounted, surface-inset, interior-radial, and interior-circumferential topologies while the stator is the same as shown in Figure 4.5:

- For the surface-mounted topology as shown in Figure 4.5a, the PMs are simply glued on the rotor surface using epoxy adhesive, thus offering the advantage of simplicity of manufacture. Since the permeability of PMs is near to that of air, the effective air-gap is the sum of the actual air-gap length and the radial thickness of the PMs. Hence, the corresponding armature reaction field is small and the stator winding inductance is low. However, since the d -axis and q -axis stator winding inductances are nearly the same, its reluctance torque is almost zero. In addition, there is a possibility that the PMs may fly apart during high-speed operation.
- For the surface-inset topology as shown in Figure 4.5b, the PMs are inset on the rotor surface. Thus, the q -axis inductance becomes higher than the d -axis inductance, hence producing an additional reluctance torque. In addition, since the PMs are inset in the rotor, it can offer better mechanical integrity than the surface-mounted one to withstand the centrifugal force at high-speed operation.
- For the interior-radial topology as shown in Figure 4.5c, the PMs are radially magnetized and buried inside the rotor. Compared with the surface-inset one, this topology enables the PMs well protected from flying apart, thus further improving the mechanical integrity for high-speed operation. Also, because of its d - q saliency, an additional reluctance torque is generated. Differing from the surface-inset one, this interior-radial topology adopts linear PMs that are easier for insertion and are easily machinable.

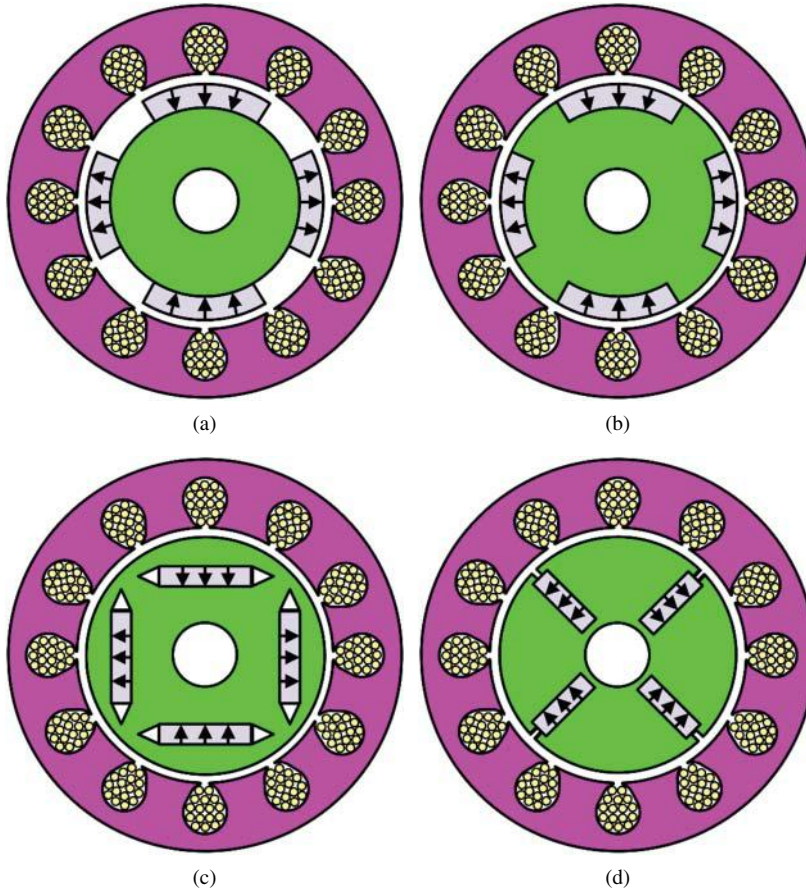


Figure 4.5 PM synchronous machine topologies: (a) surface-mounted, (b) surface-inset, (c) interior-radial, and (d) interior-circumferential

- For the interior-circumferential topology as shown in Figure 4.5d, the PMs are circumferentially magnetized and buried inside the rotor. It takes the definite advantage that the air-gap flux density can be higher than the PM remanence, the so-called flux-focusing or flux-concentration. In addition, it holds the merits of good mechanical integrity and additional reluctance torque. However, because of significant flux leakage at the inner ends of PMs, a nonmagnetic shaft or collar is generally required, which may degrade the torsional stiffness of the rotor shaft.

The above-mentioned inner-rotor PM synchronous machine topologies can readily be extended to the outer-rotor ones. The principle of operation of the outer-rotor PM synchronous machine is the same as the inner-rotor counterpart. The outer-rotor machine topology is particularly preferred to in-wheel drive because the corresponding outer rotor has a large radial diameter which can accommodate a large number of PM poles, hence offering low-speed high-torque direct-drive capability.

4.3.1.2 PM Brushless DC Machine Structure

By topologically inverting the stator and rotor of the PM DC machine, the PM BLDC machine can be generated. The key is to use electronic commutation to replace the mechanical commutation. Hence, the

most obvious advantage of the PM BLDC machine is the removal of commutator and brushes, leading to eliminate many problems associated with them.

The PM BLDC machine has a similar structure as the PM synchronous machine, namely the three-phase stator windings and PM rotor. However, the PM BLDC machine generally adopts the concentrated winding instead of the distributed winding, and has the trapezoidal air-gap flux density distribution instead of the sinusoidal flux distribution. Because of the use of concentrated windings, the end-windings can be significantly shortened, hence saving the copper material and associated copper loss. In general, the PM BLDC machine adopts the surface-mounted PM rotor as depicted in Figure 4.6, which takes the definite advantages of simplicity in both structure and control. Nevertheless, other types of PM rotors such as the surface-inset, interior-radial, and interior-circumferential topologies can also be adopted, provided the air-gap flux density distribution is close to trapezoidal; otherwise, the torque production will be deteriorated.

4.3.2 Principle of PM Brushless Machines

The principle of PM brushless machines, including the PM synchronous machine and the PM brushless machine, needs to be separately described because they are very different. That is, the principle of PM synchronous machine is based on the interaction of sinusoidal back electromotive force (EMF) waveforms and sinusoidal armature current waveforms, whereas the principle of PM BLDC machine is based on the interaction of trapezoidal back EMF waveforms and rectangular armature current waveforms.

4.3.2.1 PM Synchronous Machine Operation

The PM synchronous machine has the balanced three-phase sinusoidal distribution of air-gap flux and sinusoidal distribution of armature winding. So, the three-phase induced back EMF waveforms can be expressed as

$$e_a = E_m \sin(\omega t) \quad (4.1)$$

$$e_b = E_m \sin(\omega t - 120^\circ) \quad (4.2)$$

$$e_c = E_m \sin(\omega t - 240^\circ) \quad (4.3)$$

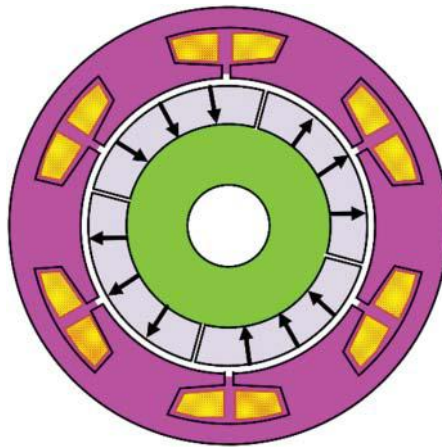


Figure 4.6 PM brushless DC machine topology

where E_m is the amplitude of back EMF waveforms and ω is the angular frequency. For proper operation, the machine is fed by balanced three-phase sinusoidal currents as given by

$$i_a = I_m \sin(\omega t - \phi) \quad (4.4)$$

$$i_b = I_m \sin(\omega t - 120^\circ - \phi) \quad (4.5)$$

$$i_c = I_m \sin(\omega t - 240^\circ - \phi) \quad (4.6)$$

where I_m is the amplitude of current waveforms and ϕ is the phase difference between the current and back EMF waveforms. Hence, as depicted in Figure 4.7, the converted electrical power can be calculated by Nam (2010) as

$$P_e = e_a i_a + e_b i_b + e_c i_c = \frac{3E_m I_m}{2} \cos \phi \quad (4.7)$$

Thus, the developed torque of this PM synchronous machine is given by

$$T_e = \frac{P_e}{\omega_r} = \frac{3E_m I_m}{2\omega_r} \cos \phi \quad (4.8)$$

which is constant at a given speed ω_r . Obviously, the developed torque can be maximized by controlling the phase difference between the armature current and back EMF waveforms to be zero.

4.3.2.2 PM Brushless DC Machine Operation

The PM BLDC machine adopts the concentrated armature winding in the stator with 120° coil span. As the PMs in the rotor cover 180° pole arc, the three-phase-induced back EMF waveforms are trapezoidal with 120° flat top regions. For proper operation, the machine is generally fed by balanced three-phase rectangular currents with 120° conduction periods, which coincide with the flat top regions of the back EMF. As depicted in Figure 4.8, each phase power is simply equal to $E_m I_m$ over the conduction period of 120° , and zero over the nonconduction period of 60° . At each instant, one phase power is equal to zero,

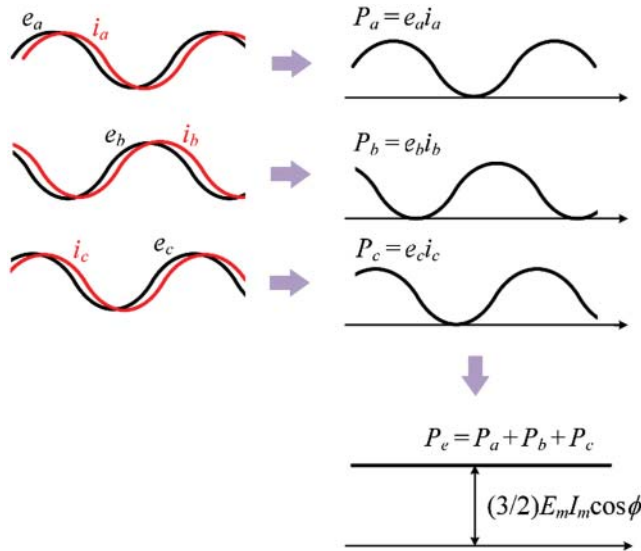


Figure 4.7 Power production of PM synchronous machine

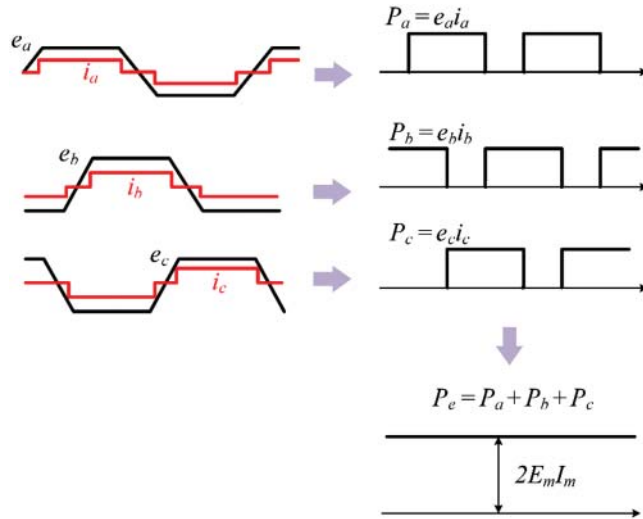


Figure 4.8 Power production of PM brushless DC machine

while the other two phases are $E_m I_m$. Hence, the converted electrical power is simply the summation of all phase powers as given by Nam (2010) as

$$P_e = e_a i_a + e_b i_b + e_c i_c = 2E_m I_m \quad (4.9)$$

Thus, the developed torque of this PM BLDC machine can be expressed as

$$T_e = \frac{P_e}{\omega_r} = \frac{2E_m I_m}{\omega_r} \quad (4.10)$$

which is constant at a given speed, ω_r . Differing from the PM synchronous machine, the PM BLDC machine produces the maximum torque naturally.

On the basis of the same current rating of the power devices for the two types of PM brushless machines, their current amplitudes are both equal to the current rating, I_p . Hence, the ratio of their power outputs (PM BLDC power to PM synchronous power) can be easily deduced from Eqs. (4.7) and (4.9) as given by

$$\text{Power ratio} = \frac{2E_m I_p}{(3/2)E_m I_p \cos \phi} = \frac{1.33}{\cos \phi} \quad (4.11)$$

which indicates that the PM BLDC machine can offer at least 33% higher power capability than the PM synchronous machine.

On the basis of the same copper loss of the armature windings for the two types of PM brushless machines (Krishnan, 2010), the current amplitude of the PM synchronous machine is I_p , whereas the current amplitude of the PM BLDC machine becomes $(\sqrt{3}/2)I_p$. Hence, the corresponding ratio of their power outputs is given by

$$\text{Power ratio} = \frac{2E_m (\sqrt{3}/2)I_p}{(3/2)E_m I_p \cos \phi} = \frac{1.15}{\cos \phi} \quad (4.12)$$

which indicates that the PM BLDC machine can offer at least 15% higher power density than the PM synchronous machine.

Therefore, the PM BLDC machine can offer higher power density and hence higher torque density than the PM synchronous machine by at least 15% or 33%.

4.3.3 Modeling of PM Brushless Machines

Because of different operating waveforms, namely sinusoidal waveforms in the PM synchronous machine and nonsinusoidal waveforms in the PM BLDC machine, the corresponding modeling techniques are fundamentally different. In essence, the PM synchronous machine prefers to employ d - q coordination transformation for modeling, whereas the PM BLDC machine prefers to use the state-space equation for modeling.

4.3.3.1 PM Synchronous Machine Modeling

Figure 4.9 depicts a basic model of the three-phase PM synchronous machine in which the stator reference axis is selected as the direction of maximum magnetomotive force (MMF) of Phase A, the direction of PM flux is chosen as the d -axis of the rotor reference frame, and the angle of the rotor q -axis with respect to the stator axis is defined as θ . The d - q frame is rotating at a speed of $\omega_e = d\theta/dt$, while the stator axes are fixed in space.

Assuming that the voltage, current, and back EMF are sinusoidal as well as the magnetic saturation, eddy currents, and hysteresis losses are negligible, the dynamic equation of this PM synchronous machine model in terms of phase variables can be expressed as (Ohm, 2000)

$$\begin{cases} v_a = Ri_a + p\lambda_a \\ v_b = Ri_b + p\lambda_b \\ v_c = Ri_c + p\lambda_c \end{cases} \quad (4.13)$$

where v_a , v_b , and v_c are the instantaneous three-phase stator voltages; i_a , i_b , and i_c are the instantaneous three-phase stator currents; R is the armature resistance; and λ_a , λ_b , and λ_c are the instantaneous three-phase flux linkages which can be written as

$$\begin{cases} \lambda_a = L_{aa}i_a + L_{ab}i_b + L_{ac}i_c + \lambda_{ma} \\ \lambda_b = L_{ab}i_a + L_{bb}i_b + L_{bc}i_c + \lambda_{mb} \\ \lambda_c = L_{ac}i_a + L_{bc}i_b + L_{cc}i_c + \lambda_{mc} \end{cases} \quad (4.14)$$

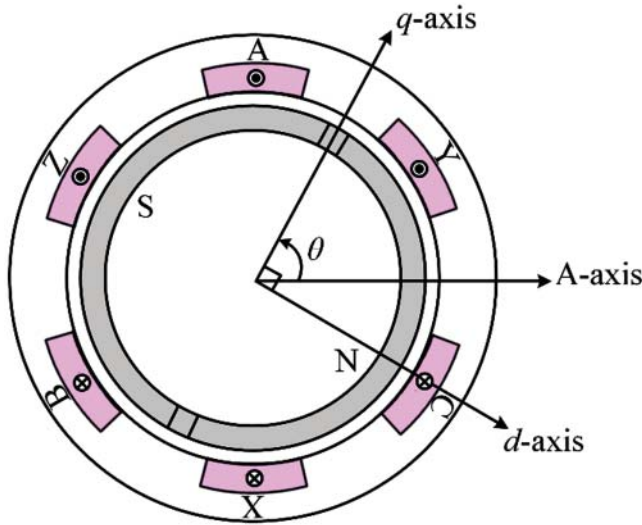


Figure 4.9 Basic model of PM synchronous machine

where L_{ij} ($i = a, b, c$ and $j = a, b, c$) are the mutual inductances which are symmetrical functions of angle θ , and λ_{ma} , λ_{mb} , and λ_{mc} are the instantaneous three-phase PM flux linkages.

By applying the Park's transformation to voltages, currents, and flux linkages in Eqs. (4.13) and (4.14), the dynamic equation can be written as

$$\begin{cases} v_d = Ri_d + p\lambda_d - \omega_e \lambda_q \\ v_q = Ri_q + p\lambda_q + \omega_e \lambda_d \end{cases} \quad (4.15)$$

where v_d and v_q are, respectively, the d -axis and q -axis components of stator voltages, i_d and i_q are, respectively, the d -axis and q -axis components of stator currents, and λ_d and λ_q are the d -axis and q -axis components of flux linkages, which can be expressed as

$$\begin{cases} \lambda_d = L_d i_d + \lambda_m \\ \lambda_q = L_q i_q \end{cases} \quad (4.16)$$

where L_d and L_q are called the d -axis and q -axis synchronous inductances, respectively and λ_m is the PM flux linkage. Substituting Eq. (4.16) into Eq. (4.15) yields

$$\begin{cases} v_d = (R + pL_d) i_d - \omega_e L_q i_q \\ v_q = (R + pL_q) i_q + \omega_e L_d i_d + \omega_e \lambda_m \end{cases} \quad (4.17)$$

which constitutes to the dynamic equivalent circuit of this PM synchronous machine as shown in Figure 4.10.

On the basis of the three-phase variables, the instantaneous input power P_i of this machine is given by

$$P_i = v_a i_a + v_b i_b + v_c i_c \quad (4.18)$$

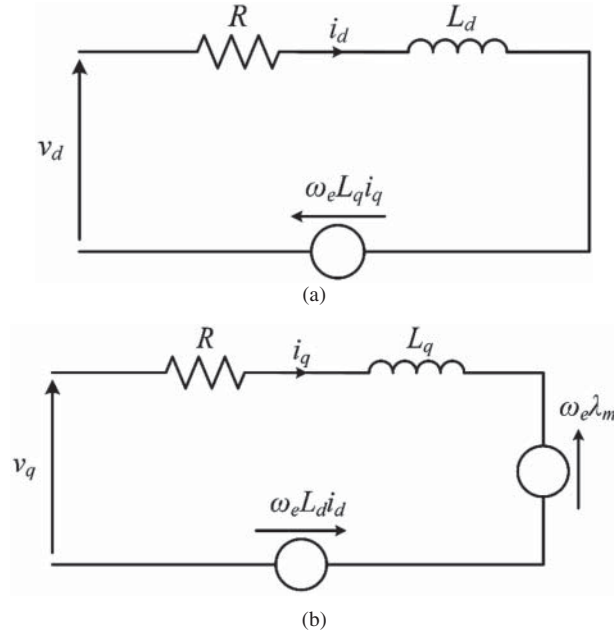


Figure 4.10 Equivalent circuit of PM synchronous machine

which can be written in terms of d -axis and q -axis variables as

$$P_i = \frac{3}{2}(v_d i_d + v_q i_q) \quad (4.19)$$

The output power P_o can be obtained by replacing v_d and v_q in Eq. (4.19) with the relevant voltages in Eq. (4.17) and flux linkages in Eq. (4.16), which yields

$$P_o = \frac{3}{2}(-\omega_e \lambda_q i_d + \omega_e \lambda_d i_q) \quad (4.20)$$

Hence, the developed torque T_e is the output power divided by the mechanical speed of $\omega_r = \omega_e / (P/2)$ as given by

$$T_e = \frac{3}{2} \frac{P}{2} (\lambda_m i_q + (L_d - L_q) i_d i_q) \quad (4.21)$$

where P is the number of poles. It can be observed that the developed torque is composed of two torque components. The first component corresponds to the reaction torque between the PM flux and q -axis armature current, while the second component corresponds to the reluctance torque due to the difference between d -axis and q -axis inductances.

4.3.3.2 PM Brushless DC Machine Modeling

Figure 4.11 shows the operating waveforms of the three-phase PM BLDC machine in which the back EMF waveforms are trapezoidal, rather than sinusoidal. Thus, the d - q modeling technique developed for the PM synchronous machine is not applicable. Since the flux linkage is nonsinusoidal, it is necessary to derive the model of the PM brushless machine in terms of its state variables.

Assuming that the rotor-induced currents due to the stator harmonics are negligible, the dynamic equation of this PM BLDC machine model can be expressed as (Pillay and Krishnan, 1988)

$$\begin{bmatrix} v_a \\ v_b \\ v_c \end{bmatrix} = \begin{bmatrix} R & 0 & 0 \\ 0 & R & 0 \\ 0 & 0 & R \end{bmatrix} \begin{bmatrix} i_a \\ i_b \\ i_c \end{bmatrix} + p \begin{bmatrix} L_{aa} & L_{ab} & L_{ac} \\ L_{ab} & L_{bb} & L_{bc} \\ L_{ac} & L_{bc} & L_{cc} \end{bmatrix} \begin{bmatrix} i_a \\ i_b \\ i_c \end{bmatrix} + \begin{bmatrix} e_a \\ e_b \\ e_c \end{bmatrix} \quad (4.22)$$

where v_a , v_b , and v_c are the instantaneous three-phase stator voltages; i_a , i_b , and i_c are the instantaneous three-phase stator currents; e_a , e_b , and e_c are the instantaneous three-phase back EMFs; R is the armature

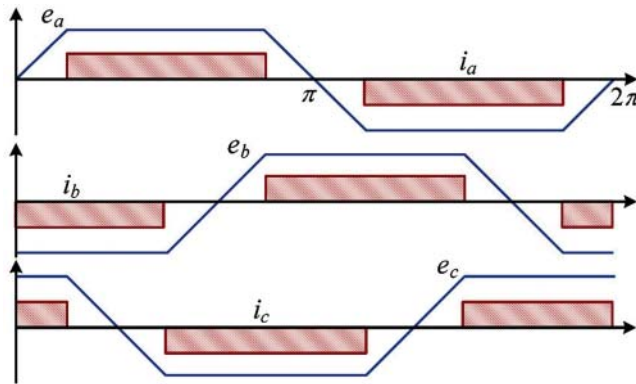


Figure 4.11 Operating waveforms of PM brushless DC machine

resistance; and L_{ij} ($i = a, b, c$ and $j = a, b, c$) are the mutual inductances which are symmetrical. As the PM BLDC machine generally adopts the surface-mounted PMs, there is no variation in the rotor reluctance with respect to the position. Hence, the self-inductances of all phases are equal to L , and the mutual inductances between phases are the same and equal to M . The dynamic equation can be written as

$$\begin{bmatrix} v_a \\ v_b \\ v_c \end{bmatrix} = \begin{bmatrix} R & 0 & 0 \\ 0 & R & 0 \\ 0 & 0 & R \end{bmatrix} \begin{bmatrix} i_a \\ i_b \\ i_c \end{bmatrix} + \begin{bmatrix} L & M & M \\ M & L & M \\ M & M & L \end{bmatrix} p \begin{bmatrix} i_a \\ i_b \\ i_c \end{bmatrix} + \begin{bmatrix} e_a \\ e_b \\ e_c \end{bmatrix} \quad (4.23)$$

Since $i_a + i_b + i_c = 0$, it yields $M i_b + M i_c = -M i_a$. Thus, the dynamic equation can be rewritten as

$$\begin{bmatrix} v_a \\ v_b \\ v_c \end{bmatrix} = \begin{bmatrix} R & 0 & 0 \\ 0 & R & 0 \\ 0 & 0 & R \end{bmatrix} \begin{bmatrix} i_a \\ i_b \\ i_c \end{bmatrix} + \begin{bmatrix} (L-M) & 0 & 0 \\ 0 & (L-M) & 0 \\ 0 & 0 & (L-M) \end{bmatrix} p \begin{bmatrix} i_a \\ i_b \\ i_c \end{bmatrix} + \begin{bmatrix} e_a \\ e_b \\ e_c \end{bmatrix} \quad (4.23)$$

which indicates that the phase voltage equation of this PM BLDC machine is similar to the armature voltage equation of the PM DC machine. Consequently, the equivalent circuit of this PM BLDC machine is depicted in Figure 4.12. Considering that all three phases are balanced and identical, a simplified equivalent circuit of one phase is shown in Figure 4.13, where $L_l = (L - M)$ is the leakage inductance.

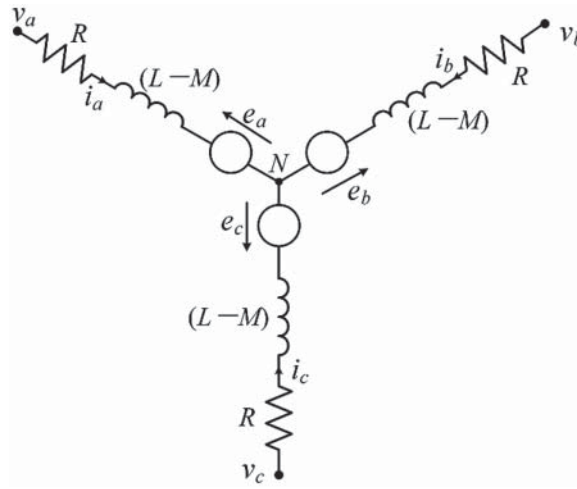


Figure 4.12 Equivalent circuit of PM brushless DC machine

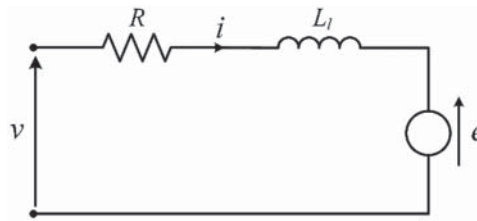


Figure 4.13 Simplified equivalent circuit of PM brushless DC machine

The developed torque T_e is the output power divided by the mechanical speed, which is given by

$$T_e = \frac{P_e}{\omega_r} = \frac{P}{2} \left(\frac{e_a i_a + e_b i_b + e_c i_c}{\omega_e} \right) \tag{4.24}$$

where P is the number of poles. As each phase back EMF is a bipolar trapezoidal waveform displaced by 120° (electrical), each current waveform needs to be 120° on positive and 120° on negative within a period to ensure the synchronism and hence produce the desired steady torque without torque pulsations.

4.4 Inverters for PM Brushless Motors

While the PM synchronous motor and PM BLDC motor are fed by sinusoidal current and rectangular current, respectively, the corresponding inverter topologies are essentially the same – a three-phase full-bridge inverter. Nevertheless, their switching schemes are different, namely the pulse-width modulation (PWM) control for BLAC operation of the PM synchronous motor, and the stepwise control for BLDC operation of the PM BLDC motor.

4.4.1 Inverter Requirements

EV propulsion requires the motor drives offering four-quadrant characteristics for forward motoring, forward regeneration, backward motoring, and backward regeneration. The definition of four quadrants and the corresponding torque-speed characteristics are summarized in Table 4.2. Particularly, the forward regeneration is essential to capture the braking energy which in turn charges the EV battery, leading to increase the driving range per charge by over 10%.

Figure 4.14 shows the schematic of the permanent magnet brushless (PMBL) AC or DC motor drive where the input voltage is the battery voltage, V_{dc} , the input DC current I_{dc} is bidirectional, the motor speed depends on the stator frequency, and its polarity is governed by the phase sequence. When the motor drive operates at Quadrant I for forward motoring, the torque and speed are positive so that the input and output powers of the inverter are positive. Thus, the average input DC current to the inverter has to be positive since the battery voltage is naturally positive. As the motor speed is positive, the phase sequence of the stator terminals is positive, namely, A-B-C. When the motor drive operates at Quadrant IV for forward

Table 4.2 Four-quadrant operation

	Quadrant	Torque	Speed
Forward motoring	I	Positive	Positive
Backward regeneration	II	Positive	Negative
Backward motoring	III	Negative	Negative
Forward regeneration	IV	Negative	Positive

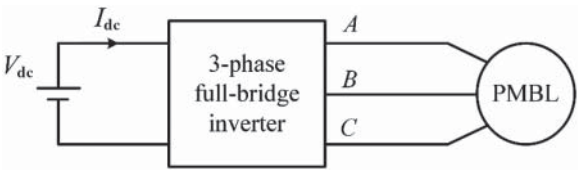


Figure 4.14 Schematic of PM brushless motor drive

Table 4.3 Inverter requirements for four-quadrant operation

	Quadrant	DC current	AC sequence
Forward motoring	I	Positive	Positive
Backward regeneration	II	Negative	Negative
Backward motoring	III	Positive	Negative
Forward regeneration	IV	Negative	Positive

regeneration, the speed is positive but the torque is negative so that the input and output powers of the inverter are negative. Thus, the average input DC current becomes negative so that the braking energy is converted to charge the battery. As the motor speed is still positive, the stator phase sequence is positive. The operations at Quadrants III and II are similar to that at Quadrants I and IV, respectively, except that the motor speed is negative and the corresponding stator phase sequence is negative, namely, A-C-B. The input DC current and stator AC phase sequence for four-quadrant operation of the PM BLAC or BLDC motor drive are summarized in Table 4.3.

4.4.2 Switching Schemes for Brushless AC Operation

The power inverter topology used for the PM synchronous motor drive operating at the BLAC mode for EV propulsion is essentially the same as that for the induction motor drive. That is, the preferred power inverter is based on the voltage-fed full-bridge topology. As the inverter has to act on the commands of magnitude, frequency, and phase of the output voltages and currents, there are various switching schemes to achieve such control. Among them, the hysteresis current control and space-vector modulation are widely used for the PM synchronous motor drive. Detailed discussion of these two PWM switching schemes can be found in Section 3.3.1.

In the hysteresis current control scheme, the actual current is forced to track the reference current within a hysteresis band. The switching frequency and peak-to-peak current ripple are governed by the width of the hysteresis band. When the width of the hysteresis band increases, the switching frequency decreases but the current ripple increases. On the other hand, when the hysteresis band decreases, the switching frequency increases whereas the current ripple decreases, leading to a more sinusoidal current waveform but associated with a higher switching loss. As a result, the width of the hysteresis band has to be properly selected to compromise between the current harmonics and switching loss. Since the hysteresis current control has the advantages of simple to implement, fast transient response, direct limitation of device current, and practical insensitivity to machine parameters, it is widely adopted by the PM synchronous motor drive for EV propulsion. However, its major drawbacks are the relatively high switching frequency and hence high switching loss, and the time-varying switching frequency may result in undesirable current harmonics.

In the space-vector modulation scheme, the three-phase voltage quantities (v_a, v_b, v_c) are first combined to derive a voltage space vector which is then resolved into any two adjacent active vectors: namely six active vectors $\bar{V}_1(100)$, $\bar{V}_2(110)$, $\bar{V}_3(010)$, $\bar{V}_4(011)$, $\bar{V}_5(001)$, $\bar{V}_6(101)$ and two zero vectors $\bar{V}_0(000)$ and $\bar{V}_7(111)$. The six nonzero vectors shape the axes of a hexagonal and the two zero vectors are at the origin of the hexagon. Consequently, the voltage vector can be formulated in terms of the eight space vectors. Therefore, rather than using a separate modulator for each of the three phases, the interaction between the three phases is taken into account. The inverter not only controls the magnitude and angular velocity but also the angular position of the voltage vector. This position variable is actually the key to offer the advantages of lowering harmonics in both the output voltage and current as well as the switching loss. Compared with the hysteresis current control, the space-vector modulation is more complicated to be implemented.

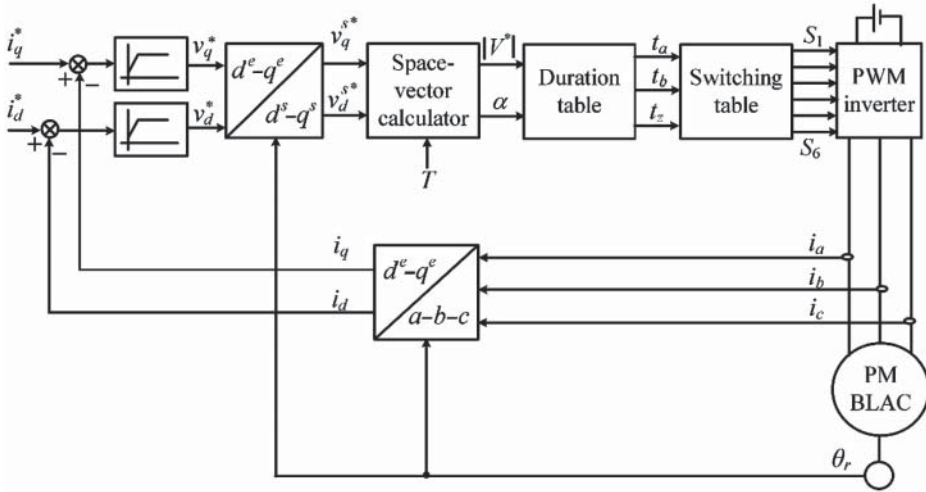


Figure 4.15 Implementation of space-vector modulation in PM synchronous motor drive

A generic implementation of space-vector modulation in the PM synchronous motor drive is shown in Figure 4.15 (Krishnan, 2010). On the basis of the errors between the d -axis and q -axis current commands and three-phase feedback currents, the d -axis and q -axis voltage commands in the rotor reference frame are resulted. After coordinate transformation, the resulting voltage commands in the stator reference frame are fed into the space-vector calculator which in turn calculates the desired magnitude and angle of the reference voltage vector at a given instant. Then, the sector is selected and the corresponding time durations of the required two switching vectors and zero vector are retrieved from a predefined table of durations. Consequently, the driving signals of power devices are extracted from another predefined table of switching devices. Notice that the sampling time T is an optional input to the space-vector calculator to enable varying the switching frequency when it is desirable.

4.4.3 Switching Schemes for Brushless DC Operation

The PM BLDC machine is driven by strokes in accordance with the rotor position. These strokes must be properly applied to the active phases of the three-phase armature winding so that the angle between the stator flux and the rotor flux is kept close to 90° to develop the maximum torque. There are two kinds of switching schemes to drive this PM BLDC machine (Safi, Acarnley, and Jack, 1995; Hu, Sathiakumar, and Shrivastava, 2009):

- Two-phase 120° conduction scheme
- Three-phase 180° conduction scheme.

In the two-phase 120° conduction scheme, at any instant, only two phases are conducted with the conduction interval of 120° while the remaining phase is nonconducted as depicted in Figure 4.16. The corresponding switching sequence is summarized in Table 4.4. For normal operation, the phase current waveform is near rectangular in shape and easily reaches the current demand as shown in Figure 4.17.

In the three-phase 180° conduction scheme, at any instant, all three phases are conducted with the conduction interval of 180° as depicted in Figure 4.18. The corresponding switching sequence is summarized in Table 4.5. For normal operation, the phase current waveform is near quasi-square in shape and easily reaches the demanded current as shown in Figure 4.19.

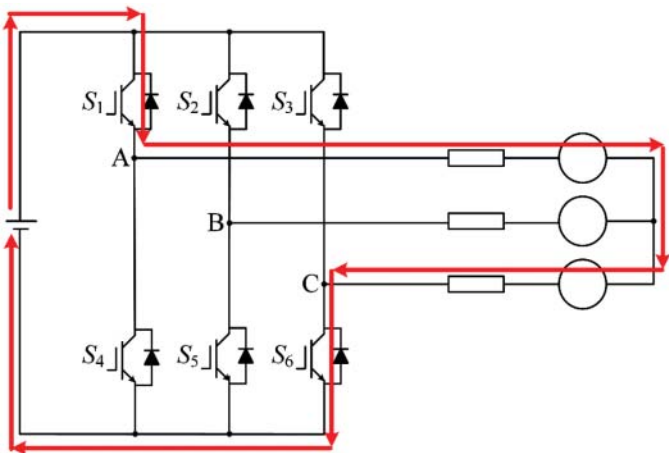


Figure 4.16 Current flow under two-phase 120° conduction scheme

Table 4.4 Switching sequence under two-phase 120° conduction scheme

Intervals (°)	Devices on	Phases A, B, C
0–60	S_1, S_6	+, 0, –
60–120	S_2, S_6	0, +, –
120–180	S_2, S_4	–, +, 0
180–240	S_3, S_4	–, 0, +
240–300	S_3, S_5	0, –, +
300–360	S_1, S_5	+, –, 0

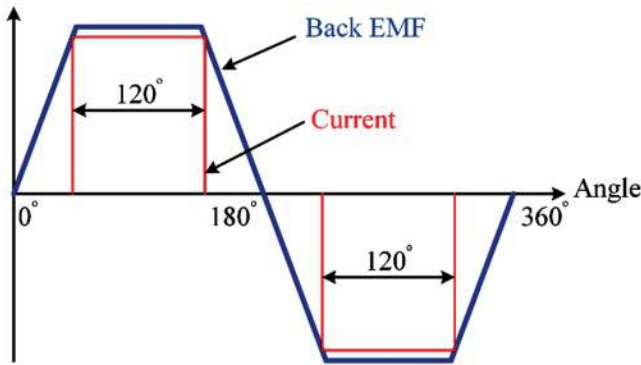


Figure 4.17 Phase back EMF and current waveforms under two-phase 120° conduction scheme

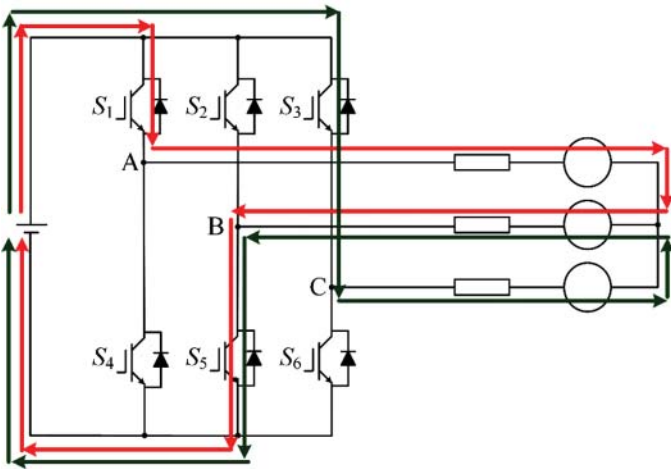


Figure 4.18 Current flow under three-phase 180° conduction scheme

Table 4.5 Switching sequence under three-phase 180° conduction scheme

Intervals (°)	Devices on	Phases A, B, C
0–60	S_1, S_5, S_3	+, −, +
60–120	S_1, S_5, S_6	+, −, −
120–180	S_1, S_2, S_6	+, +, −
180–240	S_4, S_2, S_6	−, +, −
240–300	S_4, S_2, S_3	−, +, +
300–360	S_4, S_5, S_3	−, −, +

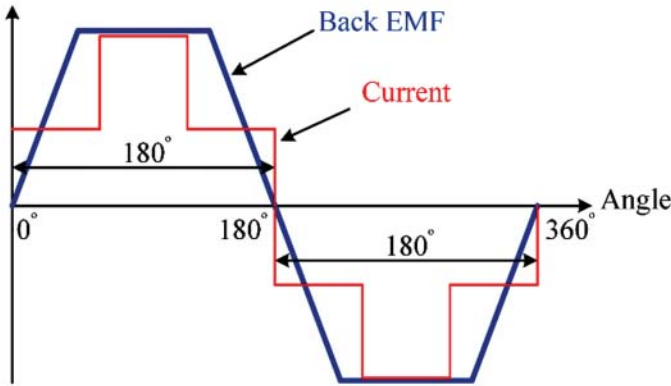


Figure 4.19 Phase back EMF and current waveforms under three-phase 180° conduction scheme

Between the 120° conduction and 180° conduction schemes, the former takes the advantage that it yields the highest torque capability for the same peak phase current which can maximize the developed torque and efficiency, whereas the latter requires only switching one device on or off in each switching sequence which can minimize the switching loss and chance of short circuit. In the 180° conduction scheme, as there are some intervals that the phase current is fed where the back EMF is not constant, the corresponding torque ripple is larger than that in the 120° conduction scheme. Therefore, the 120° conduction scheme is generally more preferable.

4.5 PM Brushless Motor Control

Since the operating waveforms of the PM synchronous and PM BLDC machines are different, the corresponding motor control strategies are naturally different. Essentially, the PM synchronous motor can adopt those control strategies that have been developed for the induction motor because both types of motors are based on sinusoidal waveforms, whereas the PM brushless motor needs to adopt dedicated control strategies because of its nonsinusoidal operating waveforms.

4.5.1 PM Synchronous Motor Control

As mentioned earlier, the PM synchronous motor can adopt those sophisticated control strategies that have been developed for the induction motor, such as the FOC and direct torque control. Between them, the FOC has been widely applied to the PM synchronous motor for EV propulsion. Meanwhile, differing from the induction motor, the PM synchronous motor adopts PM field excitation which is inherently uncontrollable. In order to provide the constant-power operation for EV cruising, the flux-weakening control of the PM synchronous motor is highly desirable. On the other hand, in order to get rid of the costly position encoder, the position sensorless control has been actively developed for the PM synchronous motor. Therefore, these three prominent control strategies will be discussed.

4.5.1.1 Field-Oriented Control of PM Synchronous Motor

The FOC of the PM synchronous motor is similar with that of the induction motor, except that their torque-production mechanisms are different. Taking into account the inertia J and viscous friction B of the entire system, the motion equation can be expressed as

$$T_e = T_l + J \frac{d\omega_r}{dt} + B\omega_r \quad (4.25)$$

where T_l is the mechanical load torque. Substituting Eqs. (4.17) and (4.21) into Eq. (4.25), the system dynamics of the PM synchronous motor in the d - q frame can be deduced as illustrated in Figure 4.20.

In order to implement the FOC, the sensed currents are first transformed from the a - b - c frame into the d - q frame. For such transformation, the flux angle θ_e is required which is deduced from the position sensor such as a position encoder or resolver. In general, the deviation between the reference speed and feedback speed is used to deduce the q -axis current reference via the speed proportional-integral (PI) regulator. Then, two PI controllers are used to regulate the d -axis current and q -axis current, hence the flux and torque, respectively (Nam, 2010). Mathematically, the corresponding v_d and v_q are given by

$$\begin{cases} v_d = G_d (i_d^* - i_d) - \omega_e L_q i_q \\ v_q = G_q (i_q^* - i_q) + \omega_e L_d i_d + \omega_e \lambda_m \end{cases} \quad (4.26)$$

where G_d and G_q are the transfer functions of relevant PI controllers. Consequently, the resulting v_d and v_q are fed into the space-vector PWM modulator to produce the desired switching signals for the power inverter. The whole block diagram of this PM synchronous machine using FOC is shown in Figure 4.21.

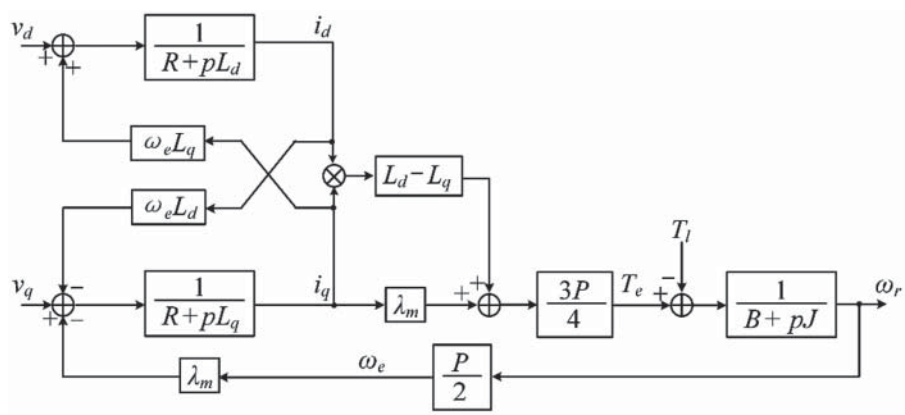


Figure 4.20 System dynamics of PM synchronous motor

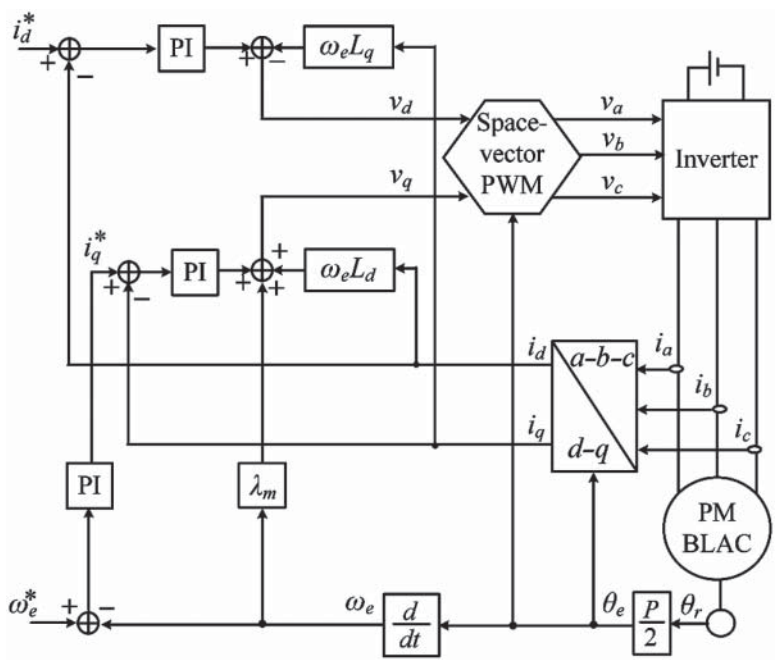


Figure 4.21 Field-oriented control of PM synchronous motor

4.5.1.2 Flux-Weakening Control of PM Synchronous Motor

At the base speed of the PM synchronous machine, the terminal voltage reaches the rated voltage. Since the back EMF grows with the speed, the speed range can only be extended by reducing the air-gap flux, the so-called flux-weakening operation. Thus, the torque decreases while the speed increases, leading to keep the power constant, the so-called constant-power operation.

In order to realize the flux-weakening control of the PM synchronous motor, the current and voltage vectors, as given by Eq. (4.17), should be controlled in such a way that the d -axis armature current is negative, while the q -axis armature current is positive. Figure 4.22 depicts the corresponding vectors when

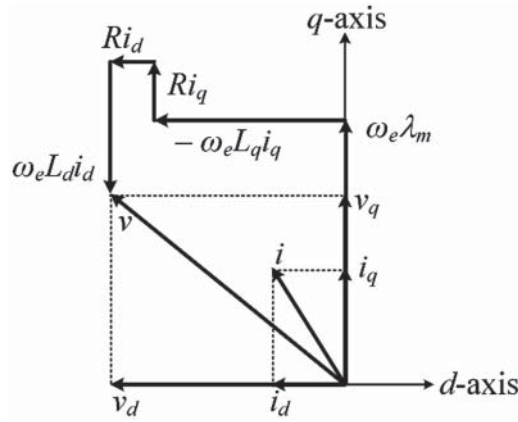


Figure 4.22 Current and voltage vectors of flux-weakening control of PM synchronous motor

$i_d < 0$ and $i_q > 0$. It can be observed that the total flux linkage and hence the back EMF can be compensated by the induced voltage with negative d -axis armature current (Schiferl and Lipo, 1990; Soong and Ertugrul, 2002). Thus, by increasing i_d in the negative direction, the back EMF can be significantly weakened.

For high-speed operation, the voltage drop across the stator resistance is negligible. Thus, the steady-state relationship of Eq. (4.17) can be written as

$$\begin{cases} v_d = -\omega_e L_q i_q \\ v_q = \omega_e L_d i_d + \omega_e \lambda_m \end{cases} \quad (4.27)$$

Taking V_r as the rated voltage limit, the d - and q -axis voltages are governed by

$$v_d^2 + v_q^2 \leq V_r^2 \quad (4.28)$$

Substituting Eq. (4.27) in Eq. (4.28) and expressing the PM flux linkage λ_m as a product of d -axis inductance L_d and a virtual field current source i_f , it yields

$$\frac{(i_d + i_f)^2}{V_r^2 / (\omega_e L_d)^2} + \frac{i_q^2}{V_r^2 / (\omega_e L_q)^2} \leq 1 \quad (4.29)$$

which represents a set of ellipses with different speeds. The higher the speed ω_e , the smaller the ellipse is resulted (Nam, 2010), leading to shrink to the center $(-i_f, 0)$ as depicted in Figure 4.23 in which the d -axis and q -axis currents are also governed by the rated current I_r as given by

$$i_d^2 + i_q^2 \leq I_r^2 \quad (4.30)$$

The intersection points of the ellipses and the circle represent the solution pairs of (i_d, i_q) to achieve the desired flux-weakening operation. It can be observed that when the speed becomes very high, the d -axis current approaches $-I_r$ while the q -axis current approaches zero. Hence, using Eq. (4.16), the criterion of offering flux-weakening operation at infinite speed can be deduced as

$$\frac{L_d I_r}{\lambda_m} = 1 \quad (4.31)$$

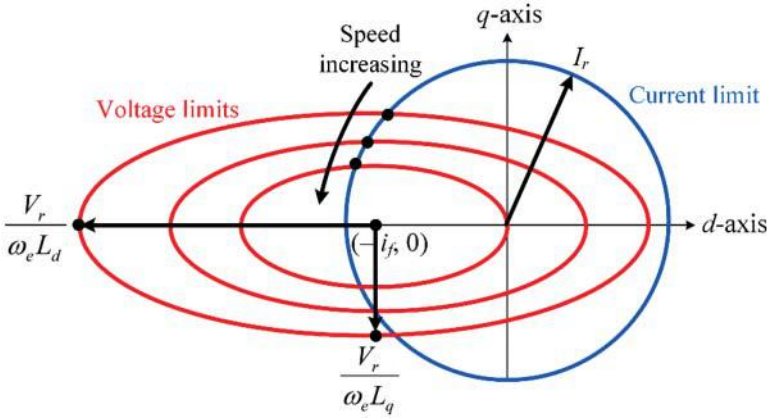


Figure 4.23 Voltage and current limits of flux-weakening control of PM synchronous motor

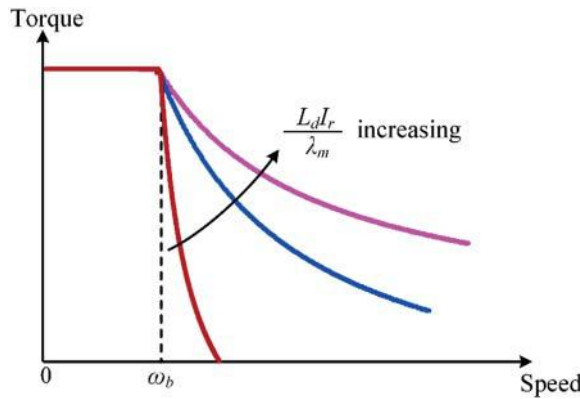


Figure 4.24 Torque-speed capabilities of flux-weakening control of PM synchronous motor

Although it is possible to design the PM synchronous motor satisfying the above criterion, it is generally with $L_d I_r / \lambda_m < 1$ because the d -axis inductance is relatively low as a consequence of the PM permeability approximately equal to unity. Figure 4.24 depicts the torque-speed capabilities of the PM synchronous motor beyond the base speed ω_b at different values of the ratio $L_d I_r / \lambda_m$. It can be found that the higher the ratio is adopted, the better the flux-weakening capability can be provided. In other words, if the PM flux linkage is set to a high value in order to achieve a high torque capability at low speeds, the speed range for flux-weakening operation will be sacrificed. On the other hand, if the rated current is very high, that is the motor is liquid cooled, the criterion Eq. (4.31) will also be satisfied even for the surface-mounted PM synchronous motor that has a low d -axis inductance and a high PM flux linkage. However, in general, it is easier for the interior PM synchronous motor to satisfy the criterion because it has a higher d -axis inductance.

4.5.1.3 Position Sensorless Control of PM Synchronous Motor

In general, the PM synchronous motor requires an accurate position sensor for the implementation of sophisticated control strategies. This position sensor is usually based on an optical encoder or a resolver,

which sometimes costs as much as a low-power machine. Hence, in recent years, the position sensorless control of the PM synchronous motor has been actively developed, especially for those cost-sensitive applications. However, the cost of position sensor for EV motor drives, especially the PM synchronous motor drive, is relatively insignificant. The precision, reliability, and maturity of position sensorless technology are of concern. Therefore, the position sensorless technology is seldom adopted by the PM synchronous motor for EV propulsion. Although the position sensorless control of the PM synchronous motor is not highly desirable for EV propulsion, the corresponding technology can be considered as a fault-tolerant control during sensor failure.

There are many position sensorless techniques that have been developed for the PM synchronous motor. These techniques can be classified by various ways (Li and Zhu, 2008). Typically, they can be classified into four main methods (Krishnan, 2010):

- Current model adaptive scheme
- External signal injection scheme
- Current model-based injection scheme
- PWM carrier component scheme

4.5.2 PM Brushless DC Motor Control

As the PM BLDC motor is driven when the stator flux and the rotor flux is kept close to 90° , it can readily produce the maximum torque per ampere in the region of constant-torque operation. This enables the PM BLDC motor taking a definite advantage over the PM synchronous motor which relies on using the $d-q$ coordinate transformation. However, in the absence of $d-q$ coordinate transformation or FOC, the control scheme for constant-power operation of the PM BLDC motor is much more complicated than that of the PM synchronous motor (Chan *et al.*, 1998). Thus, the phase-advance angle control will be discussed which can enable the PM BLDC motor offering constant-power operation for EV cruising. Meanwhile, as the position sensorless control has been actively developed for the PM BLDC motor, it will also be briefed for possible application to EVs.

4.5.2.1 Phase-Advance Angle Control of PM Brushless DC Motor

When the PM BLDC motor operates at speeds higher than the base speed, it runs out of time to enable the phase current reaching the desired level because of the small difference between the applied voltage and back EMF (Safi, Acarnley, and Jack, 1995; Chan *et al.*, 1996). At this speed, the phase current may just reach the desired level and then be turned off at the end of the conduction period. By purposely advancing the turn-on angle of the phase current, dubbed as the phase-advance angle control, the phase current can have sufficient time to rise up and keep the current in phase with the back EMF under high-speed operation. Figure 4.25 illustrates the effect of phase-advance angle control. It can be found that the constant-power operation region can be significantly extended by gradually increasing the phase-advance angle.

This phase-advance angle control can be explained by using the voltage equation of the j th phase as given by

$$v_j \left(\omega t + \theta_o - \frac{(j-1)\pi}{3} \right) = Ri_j \left(\omega t + \theta_o - \frac{(j-1)\pi}{3} \right) + L \frac{di_j}{dt} \left(\omega t + \theta_o - \frac{(j-1)\pi}{3} \right) + e_j \left(\omega t - \frac{(j-1)\pi}{3} \right) \quad (4.32)$$

where $j = 1-3$, v_j is the applied voltage, i_j is the phase current, e_j is the back EMF, R is the phase resistance, L is the phase self-inductance, and θ_o is the phase-advance angle or called the advanced conduction angle of the applied voltage leading ahead the back EMF. The control mechanism is to purposely employ

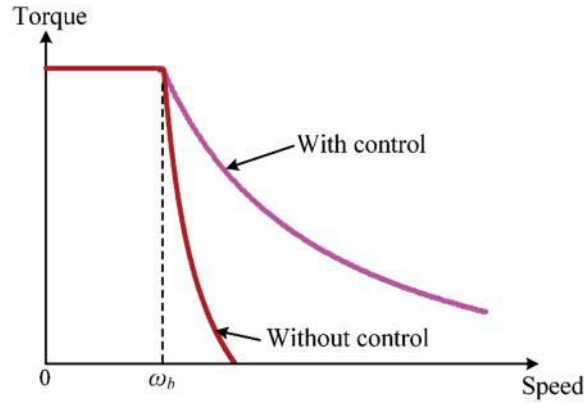


Figure 4.25 Torque-speed capabilities of phase-advance angle control of PM brushless DC motor

the inductance EMF across the phase self-inductance ($L \frac{di}{dt}$) to counteract the back EMF, which may be even larger than the applied voltage at high speeds. This inductance EMF, proportional to the derivative of phase current, is controlled by the phase-advance angle. When this angle has a suitable positive value, at the beginning of conduction with a lower back EMF, the phase current quickly rises up and the inductance EMF is positive, which indicates that electromagnetic energy is stored in the phase winding. The phase current reaches the maximum value when the back EMF equals the applied voltage. After that, the back EMF is larger than the applied voltage. The phase winding begins to release the electromagnetic energy and the phase current decreases gradually. Since the corresponding inductance EMF becomes negative, it assists the applied voltage to counteract the back EMF. By varying the phase-advance angle, the phase current waveform is shaped in such a way that the phase current is properly regulated. Therefore, this phase-advance angle control can produce an equivalent flux-weakening effect to achieve the constant-power operation of the PM BLDC motor.

Between the 120° conduction and 180° conduction schemes for the PM BLDC motor, the former takes the advantage of higher torque capability at speeds below the base speed, whereas the latter has better constant-power operation performance at speeds higher than the base speed since it virtually extends the interval for which the phase winding is excited. Figure 4.26 compares the torque-speed capabilities of the

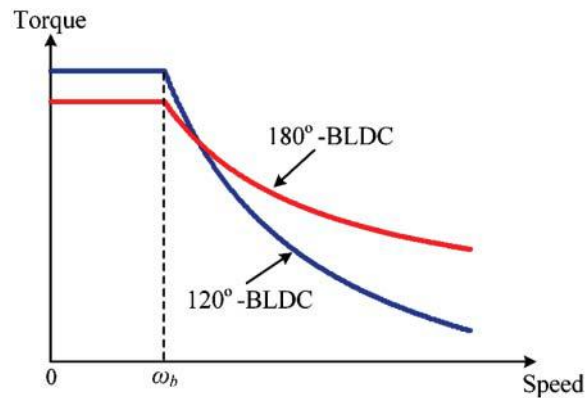


Figure 4.26 Comparison of torque-speed capabilities of two conduction schemes of PM brushless DC motor

PM BLDC motor using the 120° conduction and 180° conduction schemes with the use of phase-advance angle control for operating speeds above the base speed. It confirms that the 180° conduction scheme is more suitable for constant-power operation (Zhu and Howe, 2007).

4.5.2.2 Position Sensorless Control of PM Brushless DC Motor

Similar to the PM synchronous motor, the PM BLDC motor requires a position sensor to obtain the rotor position information in order to perform electronic commutation properly. Differing from the PM synchronous motor, which desires accurate position sensing using an encoder or a resolver, the PM BLDC motor usually requires a less demanding one, either a three-element Hall-effect or optical sensor. Thus, the position sensorless control of the PM BLDC motor is less desirable than that of the PM synchronous motor. Taking into account the fact that the cost of such position sensor is insignificant as compared with the total cost of the EV motor drive, the use of position sensorless control for the PM BLDC motor in EVs is not attractive. Nevertheless, the position sensorless technology can be considered useful for fault-tolerant control of the PM BLDC motor during sensor failure.

There are many position sensorless techniques that have been developed to estimate the commutation signals for the PM BLDC motor (Kim, Lee, and Ehsani, 2007). Typically, they can roughly be classified into five main methods (Krishnan, 2010):

- Estimation using machine model
- Induced EMF from sensing coils
- Inactive phase EMF sensing
- Third harmonic-induced EMF detection
- Artificial intelligent control.

4.6 Design Criteria of PM Brushless Motor Drives for EVs

PM brushless motors have become the preferred choice for EV propulsion because of their high efficiency and high power density. The key drawback of these motors is the expensive PM material. Thus, it is essential to use as little PM material as possible in order to reduce the cost without sacrificing the motor performance. In recent years, finite element analysis has been extensively used for PM motor designs (Rasmussen *et al.*, 2000). However, the preliminary motor dimensions should first be determined before one can proceed to finite element analysis; otherwise, the design process will be ad-hoc and tedious.

The sizing of PMs is one of the critical tasks of PM brushless motor design. Some analytical approaches have been developed to calculate the volume and size of PMs (Gieras and Wing, 2002), which can serve as a preliminary design for finite element analysis. As detailed in Mi (2006), the total PM volume V_m required for the PM synchronous machine can be estimated by

$$V_m = C_v \frac{P_1}{f B_r H_c} \quad (4.33)$$

where C_v is a coefficient which is in the range of 0.54–3.1 with a typical value of 2, P_1 is the input power, f is the supply frequency, B_r is the PM remanence, and H_c is the PM coercivity. When the motor adopts a series-magnet structure such as the surface-mounted, surface-inset, or interior-radial PM structures, the thickness (or height) h_m of each PM pole is given by

$$h_m = K_s \frac{K_a F_{ad}}{H'_c} \quad (4.34)$$

where K_s is the safety ratio, which can be chosen as 1.1, K_a is the maximum possible per-unit armature current, which is in the range of 4–8, F_{ad} is the d -axis armature reaction MMF, and H'_c is the

PM coercivity at the maximum operating temperature. On the other hand, when the motor adopts a parallel-magnet structure such as the interior-circumferential PM structure, the corresponding thickness is halved. Consequently, when the PMs are rectangular in shape, no matter for the series-magnet or parallel-magnet structure, the width (or breadth) b_m of each PM pole is given by

$$b_m = \frac{V_m}{2ph_m l_e} \quad (4.35)$$

where p is the number of pole-pairs and l_e is the effective PM length along the shaft direction, which is usually the same as the rotor stack length. If the motor adopts a series-magnet structure with arc-shaped PMs rather than rectangular PMs, the PM width will be accordingly represented by a PM radius or roughly labeled by the average width. Furthermore, for the PM BLDC machine, the volume and dimensions of PMs can be derived similarly.

The split ratio, the ratio of the stator inside diameter to the stator outside diameter, is another important design parameter for PM brushless machines, because it can significantly influence the corresponding torque capability and efficiency. The optimal split ratio for both the PM synchronous and BLDC machines has been analytically derived, which takes into account the influence of the winding disposition, air-gap flux density distribution, back EMF waveform, stator tooth-tip and end-winding (Pang, Zhu, and Howe, 2006).

When the PM brushless motor is designed to operate at the BLAC mode, it is the PM synchronous motor where the PM flux linkage and back EMF are sinusoidal. Assuming that the winding resistance is negligible, the output power P can be expressed as

$$P = \eta \frac{m}{T} \int_0^T e(t)i(t)dt = \eta \frac{m}{2} E_m I_m \quad (4.36)$$

where η is the efficiency, m is the number of phases, T is the period of back EMF, $e(t)$ and $i(t)$ are respectively the instantaneous value of back EMF and phase current, and E_m and I_m are respectively the amplitude of back EMF and phase current of the armature winding. The flux linkage of PMs on the armature winding ψ_{pm} can be expressed as

$$\psi_{pm} = \psi_m \cos(\pi\theta_r/\theta_{cr}) = \psi_m \cos(p\theta_r) \quad (4.37)$$

where ψ_m is the amplitude of PM flux linkage, θ_r is the angle of rotor position, p is the number of PM pole-pairs, and θ_{cr} is the PM pole-pitch. And, ψ_m can be expressed as

$$\psi_m = \sqrt{2} \frac{1}{p} k_w N_{ph} B D_{si} l_e \quad (4.38)$$

where k_w and N_{ph} are respectively the winding factor and number of turns of the armature winding, B is the magnetic loading, D_{si} is the stator inside diameter, and l_e is the effective axial length. Hence, e can be deduced as

$$e(t) = -d\psi_{pm}/dt = \sqrt{2} N_{ph} \omega_r k_w B l_e D_{si} \sin(p\theta_r) \quad (4.39)$$

where ω_r is the rotor speed. The corresponding amplitude E_m is given by

$$E_m = \sqrt{2} N_{ph} \omega_r k_w B l_e D_{si} \quad (4.40)$$

On the other hand, the current amplitude I_m can be deduced as

$$I_m = \frac{\sqrt{2} A \pi D_{si}}{2m N_{ph}} \quad (4.41)$$

where A is the electric loading. Therefore, based on Eqs. (4.36)–(4.41), P can be rewritten as

$$P = \frac{\pi}{2} \eta k_w ABD_{si}^2 l_e \omega_r \quad (4.42)$$

Therefore, the output torque T can be obtained as

$$T = \frac{\pi}{2} \eta k_w ABD_{si}^2 l_e \quad (4.43)$$

In order to investigate the influence of split ratio on the output torque, the magnetic and electric loadings should be expressed in terms of size parameters. Thus, the amplitude of magnetic loading B_m is expressed as

$$B_m = \frac{4}{\pi} B_{pm} \sin\left(\frac{\pi}{2} \alpha_p\right) \quad (4.44)$$

where α_p is the pole-arc factor of PMs and B_{pm} is the operating point of PMs at no load. In addition, B_{pm} is constrained by

$$h_m = \mu_r \frac{l_g}{\left(\frac{B_r}{B_{pm}} - 1\right)} \quad (4.45)$$

where μ_r is the relative permeability of PMs, B_r is the remanence of PMs, l_g is the air-gap length, and h_m is the thickness of PMs. On the other hand, the electric loading can be expressed as

$$A = \frac{JA_s k_p N_s}{\pi D_{si}} \quad (4.46)$$

where J is the stator slot current density, k_p is the slot packing factor, N_s is the number of stator slots, and A_s is the stator slot area which is given by

$$A_s = \left\{ \frac{\pi D_{so}^2}{4N_s} \left[\left(1 - \frac{2h_c}{D_{so}}\right)^2 - \left(\frac{D_{si}}{D_{so}}\right)^2 \right] - w_t \left(\frac{D_{so} - D_{si}}{2} - h_c \right) \right\} \quad (4.47)$$

where h_c is the stator yoke thickness and w_t is the stator tooth width. The tooth width and yoke thickness of the stator can be expressed as

$$w_t = h_c = \frac{1}{2} \frac{B_m}{B_{max}} \frac{D_{si}}{p} \quad (4.48)$$

where B_{max} is the maximum magnetic flux density allowable in the stator core. Substituting Eq. (4.48) into Eq. (4.47), the stator slot area can be obtained as

$$A_s = \frac{\pi D_{so}^2}{4N_s} \left\{ \left[\frac{1}{p} \left(\frac{1}{p} + \frac{N_s}{p\pi} \right) \left(\frac{B_m}{B_{max}} \right)^2 + \frac{N_s}{p\pi} \left(\frac{B_m}{B_{max}} \right) - 1 \right] \left(\frac{D_{si}}{D_{so}} \right)^2 - \left(\frac{2}{p} + \frac{N_s}{p\pi} \right) \left(\frac{B_m}{B_{max}} \right) \left(\frac{D_{si}}{D_{so}} \right) + 1 \right\} \quad (4.49)$$

And, D_{si} is constrained by

$$D_{si} = D_{sh} + 2h_r + 2h_m + 2l_g \quad (4.50)$$

where D_{sh} is the shaft diameter and h_r is the rotor yoke thickness.

Substituting Eqs. (4.44), (4.46), and (4.50) into Eq. (4.43), the variation of output torque with respect to the split ratio D_{si}/D_{so} can be obtained. In general, there is an optimal split ratio for the maximum output torque, which corresponds to a particular magnetic loading. When the PM brushless motor is designed to operate at the BLDC mode, the optimal split ratio can also be derived in a similar manner.

Recently, the double-stator PM brushless motor has been actively developed for EV application because it can offer exceptionally high torque density (Niu, Chau, and Yu, 2009). From the structural point of view, the double-stator PM brushless motor is composed of two coaxial PM brushless motors: its inner motor is an outer-rotor PM brushless motor, while its outer motor is a conventional PM brushless motor. Its total output torque is the resultant of the torque components produced by the interactions of the inner and outer armature windings with the inner and outer air-gap flux densities, respectively. Thus, the aforementioned design criteria for the optimal split ratio of a conventional PM brushless motor can readily be extended to the double-stator PM brushless motor to achieve the maximum torque density (Wang *et al.*, 2011).

4.7 Design Examples of PM Brushless Motor Drives for EVs

Because of inherently high power density and high torque density, PM brushless motor drives are particularly attractive for in-wheel drive where the usable space to accommodate the motor drive is highly limited. There are two major types of in-wheel drives: a high-speed motor coupled with a built-in reduction gear and a low-speed outer-rotor direct-drive motor. Therefore, two PM brushless motor drives, the planetary-gear PM synchronous motor drive and the outer-rotor PM BLDC motor drive, will be designed and analyzed for exemplification.

4.7.1 Planetary-Geared PM Synchronous Motor Drive

When the PM synchronous motor is designed for high-speed operation, the required size and weight can be significantly reduced, leading to achieve high power density and high torque density. Meanwhile, in order to match the motor speed and the wheel speed, a single-step planetary gear is integrated with the motor in such a way that the sun gear is coupled with the PM rotor and the ring gear is mounted with the wheel rim. Of course, the overall power density and torque density of this PM synchronous motor drive, including the high-speed motor and planetary gear, should be higher than those of a low-speed direct-drive PM synchronous motor drive.

On the basis of the requirements of a typical passenger EV, the specifications of the planetary-gear PM synchronous motor drive are listed in Table 4.6.

Aiming to have a simple and robust structure to withstand high-speed operation, the three-phase four-pole interior-radial PM synchronous machine topology is adopted. Figure 4.27 shows its exploded diagram. On the basis of the specifications, the geometric dimensions and parameters of this motor can be initialized as listed in Table 4.7.

In order to take into account the saturation and fringing effects, the finite element analysis is extensively used for PM brushless motor designs. The electromagnetic field distribution of the PM synchronous motor at the rated condition is shown in Figure 4.28. It can be observed that when the armature current density is equal to 4.2 A/mm², there is no significant magnetic saturation.

Table 4.6 Specifications of planetary-gear PM synchronous motor drive

DC voltage	360 V
Rated power	6.3 kW
Rated speed	3000 rpm
Rated torque	20 N m
Constant-torque operation	0–3000 rpm
Constant-power operation	3000–9000 rpm
Gear ratio	10 : 1

Copyright © 2015, John Wiley & Sons, Incorporated. All rights reserved.

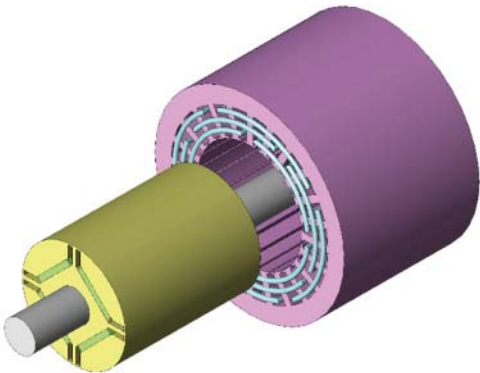


Figure 4.27 Three-phase four-pole interior-radial PM synchronous motor

Table 4.7 Initialization of PM synchronous motor design

Phase number	3
Pole number	4
Slot number	36
Stator outside diameter	140 mm
Rotor diameter	76.4 mm
Shaft diameter	22.9 mm
Air-gap length	0.3 mm
Core length	100 mm
Stator yoke thickness	12 mm
Rotor yoke thickness	7.5 mm
PM dimensions	$3.82 \times 30.6 \times 100 \text{ mm}^3$
Turns per slot	28
Slot-fill factor	60%
Lamination material	35JN210

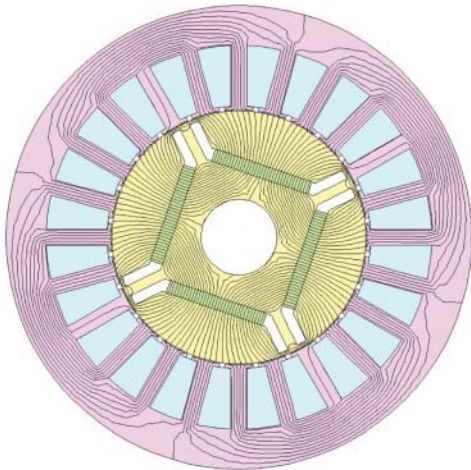


Figure 4.28 Electromagnetic field distribution of PM synchronous motor

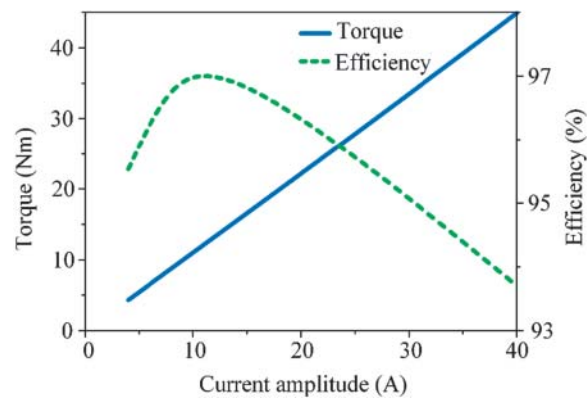


Figure 4.29 Static characteristics of torque and efficiency versus current of PM synchronous motor drive

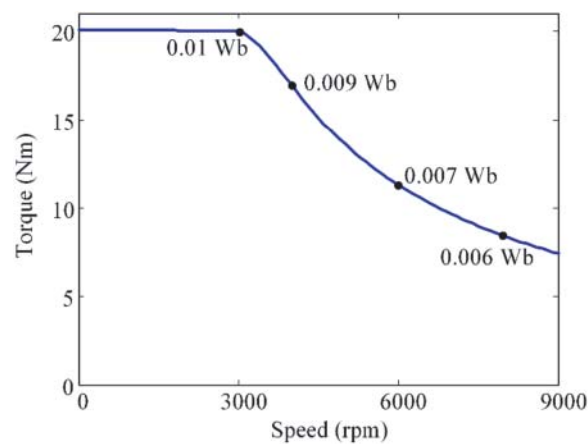


Figure 4.30 Torque-speed capability of PM synchronous motor drive

The static characteristics of the designed motor drive, namely the static torque and efficiency versus the armature current, are assessed. As plotted in Figure 4.29, when the armature current amplitude is equal to the rated value of 18.3 A, the resulting torque can reach the desired value of 20 N m. Because of the absence of rotor copper loss, the motor can maintain a high efficiency, mostly beyond 95% for normal operation. Notice that if the transmission loss of the planetary gear is taken into account, the overall efficiency will be somewhat reduced, generally still above 90%. Consequently, the operating regions of the designed motor drive, including both the constant-torque operation and constant-power operation, are assessed. The corresponding torque-speed capability is shown in Figure 4.30 in which the constant-power operation is realized by gradually weakening the air-gap flux beginning from 0.01 Wb with the increase of motor speed. It can be observed that the motor drive can provide constant-torque operation with the rated torque of 20 N m from 0 to 3000 rpm. In addition, by employing flux-weakening control, it can significantly extend the speed range for constant-power operation with the rated power of 6.3 kW from 3000 to 9000 rpm, which is highly favorable for EV application.

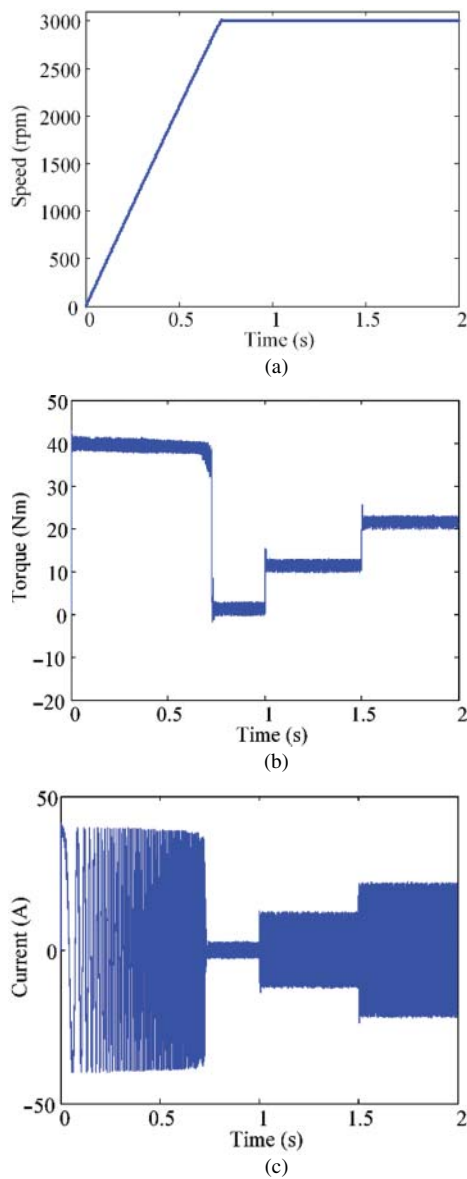


Figure 4.31 Transient responses of PM synchronous motor drive (a) speed, (b) torque, and (c) current

In order to evaluate the transient responses of the designed motor drive, it is first started up at no-load to the speed of 3000 rpm. After reaching the steady state, a half-load torque of 10 N m is suddenly applied. Then, after reaching the new steady state, a full-load torque of 20 N m is suddenly applied. As illustrated in Figure 4.31, it can be observed that the required start-up time is about 0.73 seconds, and the response time to sudden load changes is very short. In addition, the torque ripple at the rated torque is within 20%, which is very acceptable. Such low-percentage torque ripple is mainly due to the inherent feature of sinusoidal current and flux waveforms.

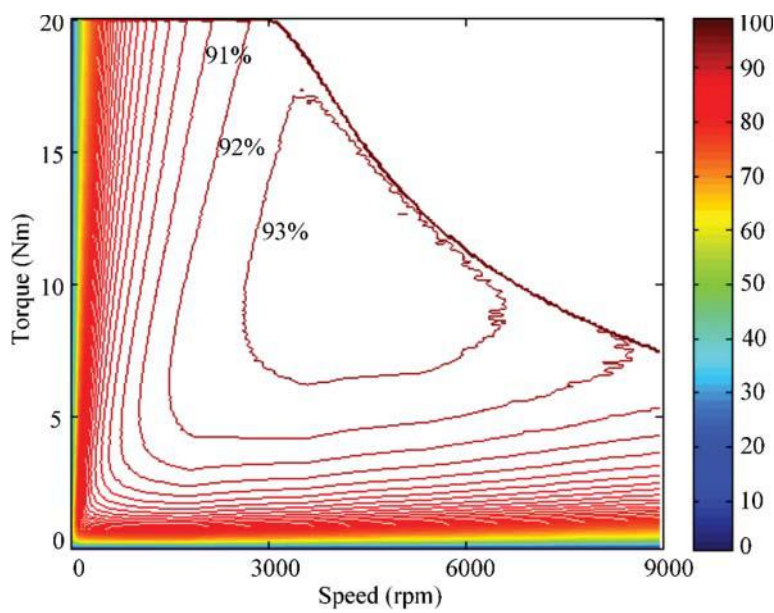


Figure 4.32 Efficiency map of PM synchronous motor drive

Differing from conventional motor drives, an EV motor drive needs to offer a good efficiency map, rather than an optimal efficiency point. The efficiency map of the designed motor drive embracing the entire operating region is plotted in Figure 4.32, where the contours on the torque-speed plane represent the operating efficiencies. It can be observed that most areas of the operating region can offer efficiencies higher than 90%, which is actually one of the key merits of the PM synchronous motor drive.

4.7.2 Outer-Rotor PM Brushless DC Motor Drive

As derived in Eqs. (4.11) and (4.12), the PM BLDC motor can offer higher power density and hence higher torque density than the PM synchronous motor by at least 15% or 33%. Hence, the PM BLDC motor is very attractive for in-wheel direct-drive application. To facilitate direct coupling between the rotor and rim, the outer-rotor PM BLDC motor drive is preferred.

On the basis of the requirements of a typical passenger EV, the specifications of the outer-rotor PM BLDC motor drive are listed in Table 4.8.

Table 4.8 Specifications of outer-rotor PM brushless DC motor drive

DC voltage	360 V
Rated power	6.3 kW
Rated speed	300 rpm
Rated torque	200 N m
Constant-torque operation	0–300 rpm
Constant-power operation	300–900 rpm

Copyright © 2015, John Wiley & Sons, Incorporated. All rights reserved.

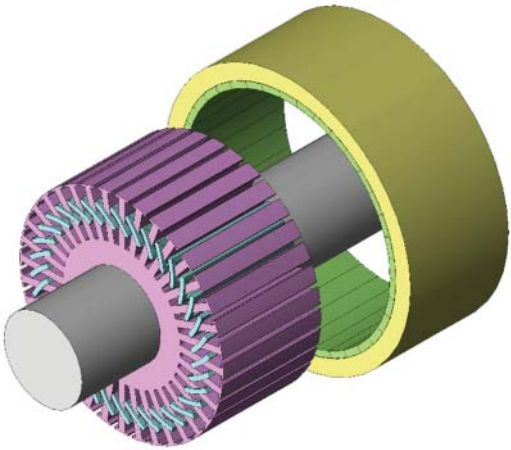


Figure 4.33 Three-phase 38-pole surface-mounted PM brushless DC motor

Table 4.9 Initialization of PM brushless DC motor design

Phase number	3
Pole number	38
Slot number	36
Rotor outside diameter	250 mm
Stator diameter	207.4 mm
Shaft diameter	80 mm
Air-gap length	0.3 mm
Core length	100 mm
Stator yoke thickness	20 mm
Rotor yoke thickness	15 mm
PM dimensions	17.7 × 6 × 100 mm ³
Turns per slot	48
Slot-fill factor	60%
Lamination material	35JN210

In order to provide the desired low-speed direct-drive operation, a large number of PM poles are required. Thus, the three-phase 38-pole surface-mounted PM BLDC machine topology is adopted. Figure 4.33 shows its exploded diagram. On the basis of the specifications, the geometric dimensions and parameters of this motor can be initialized as listed in Table 4.9. On the inner rotor surface, there are 38 PM pieces mounted alternately to form 38 poles, and two adjacent poles make up a pair of poles so that the flux paths of different pole pairs are independent. This multipole magnetic circuit arrangement enables to reduce the magnetic iron yoke, resulting in the reduction of volume and weight. The coil span of the armature winding in the stator is designed to be equal to the slot pitch, thus the end-winding and hence copper material can be significantly reduced, leading to further reduction of volume and weight. By using the fractional number of slots per pole per phase, the magnetic force between the stator and rotor at any rotating position is uniform, thus minimizing the cogging torque that usually occurred in PM BLDC motors (Wang *et al.*, 2002).

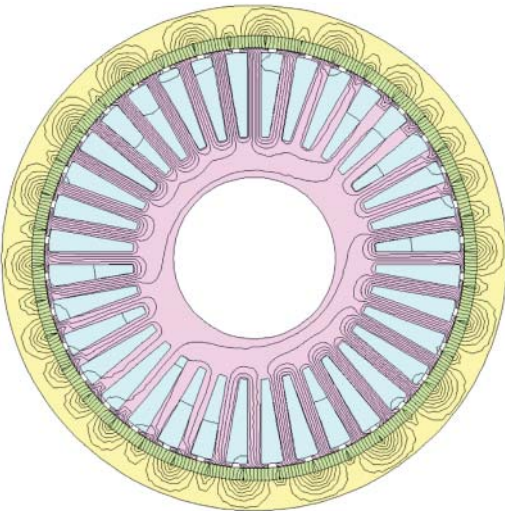


Figure 4.34 Electromagnetic field distribution of PM brushless DC motor

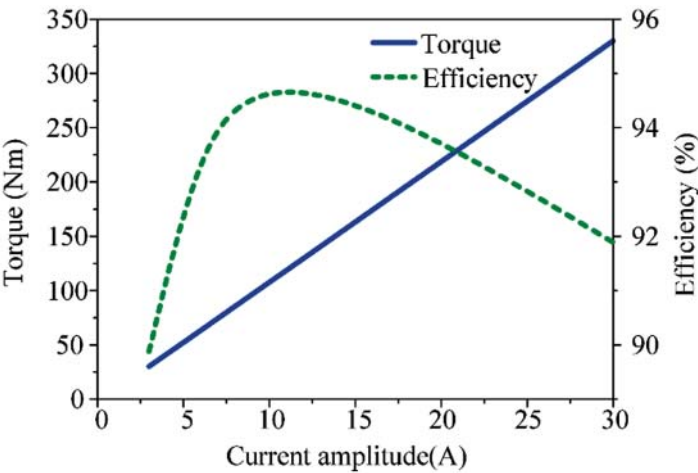


Figure 4.35 Static characteristics of torque and efficiency versus current of PM brushless DC motor drive

Firstly, the electromagnetic field distribution of the PM BLDC motor at the rated condition is analyzed as shown in Figure 4.34. It can be observed that when the armature current density is equal to 5.7 A/mm^2 , there is no significant magnetic saturation. Then, the static torque and efficiency versus the armature current amplitude are plotted in Figure 4.35. It can be found that when the armature current amplitude is equal to the rated value of 18.2 A , the resulting torque can reach the desired value of 200 N m . Meanwhile, the motor can maintain a high efficiency, mostly beyond 90% , for normal operation. It should be noted that the efficiency of this PM BLDC motor drive is slightly lower than the previous PM synchronous motor drive because of the higher copper loss under the low-speed design. Nevertheless, because of the absence of gear loss, the overall efficiency of this PM BLDC motor drive is similar to that of the previous PM synchronous motor drive.

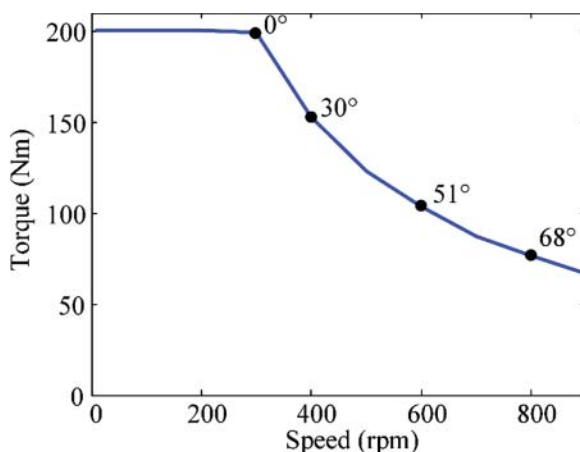


Figure 4.36 Torque-speed capability of PM brushless DC motor drive

Consequently, the torque-speed capability of the designed motor drive, including both the constant-torque operation and constant-power operation, is shown in Figure 4.36. It can be found that the motor drive can provide constant-torque operation with the rated torque of 200 N m from 0 to 300 rpm, and constant-power operation with the rated power of 6.3 kW from 300 to 900 rpm. Meanwhile, by using the phase-advance angle control, the motor drive can significantly extend the speed range for constant-power operation, which is highly favorable for EV application.

The transient responses of the designed PM BLDC motor drive is shown in Figure 4.37, where the motor is first started up at no-load to the speed of 300 rpm, then to a sudden half-load torque of 100 N m, and finally to a sudden full-load torque of 200 N m. It can be observed that the required start-up time and the response time to sudden load changes are very short. It should be noted that the required start-up time of this PM BLDC motor drive is much shorter than that of the previous PM synchronous motor drive, which is simply due to its much larger starting torque under the same no-load torque. When taking into account the gearing effect, their response times should be similar. On the other hand, it can be found that the torque ripple of the PM BLDC motor is higher than that of the previous PM synchronous motor drive, which is actually due to the finite time for nonideal rectangular current commutation.

Finally, the efficiency map of the designed PM BLDC motor drive embracing the entire operating region is plotted in Figure 4.38. As expected, most areas of the operating region can offer efficiencies higher than 90%, which is highly desirable for EV propulsion.

4.8 Application Examples of PM Brushless Motor Drives in EVs

The Nissan Leaf, which stands for a Leading, Environmentally friendly, Affordable, Family car, is a five-door hatchback EV introduced by Nissan in 2010 as shown in Figure 4.39. Currently, it has the largest market share of worldwide EVs sold since 2010. Using its on-board 24 kWh lithium-ion battery, it can offer a driving range of 135 km per charge based on the US Environmental Protection Agency (EPA) profile. The corresponding propulsion system adopts an 80 kW and 254 N m front-axle PM synchronous motor drive (Nissan, 2014). With the single-speed transmission, it can offer the top speed of over 150 km/h.

The Smart Fortwo Electric Drive (ED) was launched in 2007, which is an electric version of the conventional Smart Fortwo. Daimler AG plans to mass-produce it with availability in major markets worldwide. As shown in Figure 4.40, it features a 55 kW PM BLDC motor drive, which can offer the top speed of 120 km/h with the single-speed transmission (Millikin, 2011). On the basis of a lithium-ion battery pack of

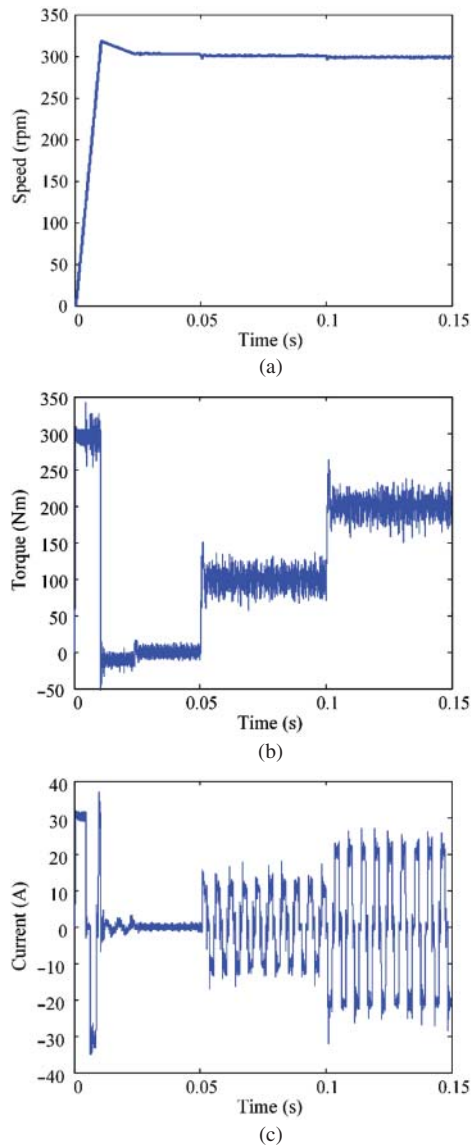


Figure 4.37 Transient responses of PM brushless DC motor drive: (a) speed, (b) torque, and (c) current

17.6 kWh, it can run 140 km per charge. With the torque of 130 N m, it can accelerate from 0 to 100 km/h in 11.5 seconds, which is essentially on par with that of the conventional Smart Fortwo.

4.9 Preferred Technology for EVs?

Among the three main types of commercially available EV motor drives, namely the DC, induction, and PM brushless, the PM brushless motor drives take the definite advantages of higher efficiency, higher power density, and higher torque density, which are highly desirable for EV propulsion. Currently, there is no doubt that the PM brushless motor drives are the preferred technology for EVs.

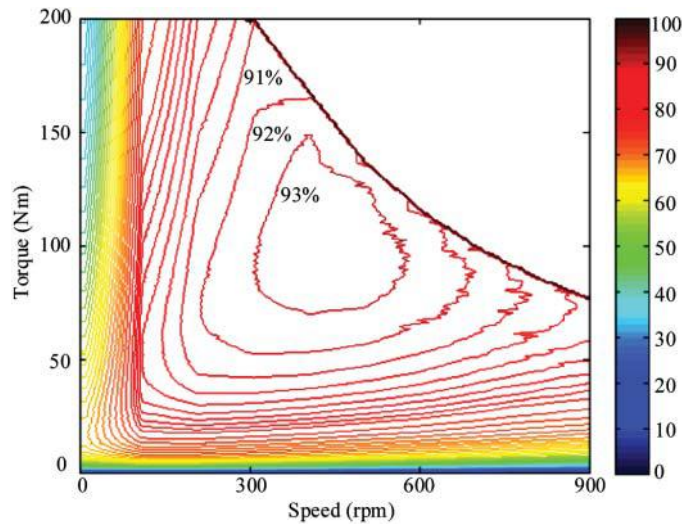


Figure 4.38 Efficiency map of PM brushless DC motor drive



Figure 4.39 Nissan Leaf

Between the two members of PM brushless motor drives, the PM synchronous motor drive is more mature than the PM BLDC motor drive while they have their individual merits. That is, the PM synchronous motor drive has relatively higher efficiency and lower torque ripple, whereas the PM BLDC motor drive has relatively higher power density and higher torque density. It is anticipated that both members will equally share the market of PM brushless motor drives.

The development of PM brushless motor drives heavily depends on the PM materials. In recent years, because of the high initial cost, shortage of supply, and thermal stability problem of PM materials, the rapid development of PM brushless motor drives has been quenched, leading to open up two new research and development directions for EV motor drives: the stator-PM motor drives and advanced magnetless motor drives. Nevertheless, the development of PM brushless motor drives is being further extended to the double-stator topologies to achieve exceptionally high torque density for EVs or the double-rotor topologies to achieve power splitting for hybrid EVs.



Figure 4.40 Smart Fortwo ED (Source: Courtesy Wikimedia Commons, http://en.wikipedia.org/wiki/Smart_Fortwo_ed#mediaviewer/File:2013_Smart_Fortwo_Electric_Drive_--_2012_NYIAS.JPG)

References

- Chan, C.C., Chau, K.T., Jiang, J.Z. *et al.* (1996) Novel permanent magnet motor drives for electric vehicles. *IEEE Transactions on Industrial Electronics*, **43**, 331–339.
- Chan, C.C., Xia, W., Jiang, J.Z. *et al.* (1998) Permanent-magnet brushless drives. *IEEE Industry Applications Magazine*, **4**, 16–22.
- Gieras, J.F. and Wing, M. (2002) *Permanent Magnet Motor Technology: Design and Applications*, 2nd, Revised and Expanded edn, Marcel Dekker, Inc., New York.
- Gutfleisch, O. (2000) Controlling the properties of high energy density permanent magnetic materials by different processing routes. *Journal of Physics D: Applied Physics*, **33**, R157–R172.
- Hu, B., Sathiakumar, S., and Shrivastava, Y. (2009) 180-degree commutation system of permanent magnet brushless DC motor drive based on speed and current control. Proceedings of International Conference on Intelligent Computation Technology and Automation, pp. 723–726.
- Kim, T., Lee, H.W. and Ehsani, M. (2007) Position sensorless brushless DC motor/generator drives: review and future trends. *IET Electric Power Applications*, **1**, 557–564.
- Krishnan, R. (2010) *Permanent Magnet Synchronous and Brushless DC Motor Drives*, CRC Press, Boca Raton, FL.
- Li, Y. and Zhu, H. (2008) Sensorless control of permanent magnet synchronous motor – A survey. Proceedings of IEEE Vehicle Power and Propulsion Conference, pp. 1–8.
- Mi, C.C. (2006) Analytical design of permanent-magnet traction-drive motors. *IEEE Transactions on Magnetics*, **42**, 1861–1866.
- Millikin, M. (2011) Third-generation smart fortwo electric drive to launch worldwide in spring 2012; first use of battery packs from Daimler JV Deutsche Accumotive and motor from JV EM-motive. Green Car Congress, <http://www.greencarcongress.com/2011/08/smart-20110816.html> (accessed September 2014).
- Nam, K.H. (2010) *AC Motor Control and Electric Vehicle Applications*, CRC Press, Boca Raton, FL.
- Nissan (2014) 2015 Nissan LEAF, Nissan, <http://www.nissanusa.com/electric-cars/leaf/> (accessed September 2014).
- Niu, S., Chau, K.T. and Yu, C. (2009) Quantitative comparison of double-stator and traditional permanent magnet brushless machines. *Journal of Applied Physics*, **105**, 07F105-1–07F105-3.
- Ohm, D.Y. (2000) *Dynamic Model of PM Synchronous Motors*, Drivetech, pp. 1–10.
- Pang, Y., Zhu, Z.Q. and Howe, D. (2006) Analytical determination of optimal split ratio for permanent magnet brushless motors. *IEE Electric Power Applications*, **153**, 7–13.
- Pillay, P. and Krishnan, R. (1988) Modeling of permanent magnet motor drives. *IEEE Transactions on Industrial Electronics*, **35**, 537–541.

- Rasmussen, K.F., Davies, J.H., Miller, T.J.E. *et al.* (2000) Analytical and numerical computation of air-gap magnetic fields in brushless motors with surface permanent magnets. *IEEE Transactions on Industry Applications*, **36**, 1547–1554.
- Safi, S.K., Acarnley, P.P. and Jack, A.G. (1995) Analysis and simulation of the high-speed torque performance of brushless DC motor drives. *IEE Proceedings – Electric Power Applications*, **142**, 191–200.
- Schiferl, R.F. and Lipo, T.A. (1990) Power capability of salient pole permanent magnet synchronous motors in variable speed drive application. *IEEE Transactions on Industry Applications*, **26**, 115–123.
- Soong, W.L. and Ertugrul, N. (2002) Field-weakening performance of interior permanent-magnet motors. *IEEE Transactions on Industry Applications*, **38**, 1251–1258.
- Wang, Y., Chau, K.T., Chan, C.C. and Jiang, J.Z. (2002) Transient analysis of a new outer-rotor permanent-magnet brushless DC drive using circuit-field-torque time-stepping finite element method. *IEEE Transactions on Magnetics*, **38**, 1297–1300.
- Wang, Y., Cheng, M., Chen, M. *et al.* (2011) Design of high-torque-density double-stator permanent magnet brushless motors. *IET Electric Power Applications*, **5**, 317–323.
- Zhu, Z.Q. and Howe, D. (2007) Electrical machines and drives for electric, hybrid, and fuel cell vehicles. *Proceedings of the IEEE*, **95**, 746–765.